The membrane-actin linkers ezrin, radixin, and moesin are dispensable for macrophage migration and cortex mechanics.

Perrine Verdys[1,2], Javier Rey Barroso[1], Joseph Vermeil[3], Martin Bergert[4], Thibaut Sanchez[1], Arnaud Métais[1], Thomas Mangeat[5], Elisabeth Bellard[1,6], Claire Bigot[1], Jean-Philippe Girard[1,6], Isabelle Maridonneau-Parini[1], Christel Vérollet[1], Frédéric Lagarrigue[1], Alba Diz-Muñoz[4], Julien Heuvingh[3], Matthieu Piel[7], Olivia Du Roure[3], Véronique Le Cabec[1,#], Sébastien Carréno[2,#], Renaud Poincloux[1,#]

[1] Institut de Pharmacologie et de Biologie Structurale (IPBS), Université de Toulouse, CNRS, Université Toulouse III - Paul Sabatier (UT3), Toulouse, France

[2] Institut de Recherche en Immunologie et en Cancérologie (IRIC), Université de Montréal, Montréal, Canada

[3] ESPCI Paris, PSL University, CNRS, Université Paris, Sorbonne Université, Paris, France

[4] Cell Biology and Biophysics Unit, European Molecular Biology Laboratory, Heidelberg, Germany

[5] LITC Core Facility, Centre de Biologie Intégrative, Université de Toulouse, CNRS, UPS, 31062 Toulouse, France

[6] Equipe Labellisée Ligue Contre le Cancer

[7] Institut Curie and Institut Pierre Gilles de Gennes, PSL University, CNRS, Paris, France

[#] co-corresponding authors

Correspondence: sebastien.carreno@umontreal.ca; veronique.le-cabec@ipbs.fr and renaud.poincloux@ipbs.fr

Abstract

The cellular actin cortex provides crucial mechanical support and plays critical roles in numerous functions, including cell division and migration. The proteins of the ERM family, ezrin, radixin, and moesin, are central to these processes by linking the plasma membrane to the actin cytoskeleton. To investigate the individual contributions of these three proteins to leukocyte migration, we generated single and triple ERM knock-out macrophages. Surprisingly, we found that even in the absence of ERMs, macrophages can still form the different actin structures promoting cell migration, such as filopodia, lamellipodia, podosomes, and ruffles. Furthermore we discovered that, unlike every other cell type previously investigated, the single or triple knock-out of ERMs does not affect macrophage migration in a large diversity of contexts. Finally, we demonstrated that the loss of ERMs in macrophages does not affect the mechanics of their actin cortex. These findings challenge the notion that

ERMs are universally essential for cortex mechanics and cell migration and support the notion that the macrophage cortex may have diverged from that of other cells to allow for their adaptive cortical plasticity.

Introduction

The actin cytoskeleton plays a major role to support the cell shape changes necessary for diverse biological processes such as morphogenesis, mitosis, phagocytosis and cell migration. The cellular cortex is organized in a thin actomyosin layer located just beneath the plasma membrane. The precise organization and regulation of this dynamic structure is critical for physiological processes, as disruptions of the actin cortex have been linked to different pathologies, such as cancer (Chugh and Paluch, 2018). Membrane-cortex attachment is essential for the regulation of mechanical properties and dynamics of the cortex, essential for processes such as mitosis (Carreno et al., 2008; Kunda et al., 2012, 2008; Leguay et al., 2022; Roch et al., 2010; Roubinet et al., 2011) or the formation of actin-driven and bleb-based protrusions during cell migration (Diz-Muñoz et al., 2010; Welf et al., 2020). Ezrin, radixin and moesin compose the ERM protein family and are one of the main mechanical linkers between the plasma membrane and the actin cytoskeleton (Bretscher, 1983; Bretscher et al., 1997; Lankes and Furthmayr, 1991; Tsukita et al., 1989).

As such, ERM activation at mitotic entry was shown to promote rounding of metaphase cells by increasing stiffening of the cortex (Kunda et al., 2008; Larson et al., 2010; Leguay et al., 2022). By solidifying the actin-to-membrane link, ERMs also increase membrane tension in mesendodermal progenitors of zebrafish embryos, epithelial cells, and lymphocytes (Diz-Muñoz et al., 2010; Liu et al., 2012; Rouven Brückner et al., 2015; Tsujita et al., 2021). Having a key role in the link between the plasma membrane and the actomyosin cortex, ERMs control the organization and dynamics of thin actin structures such as brush border microvilli of epithelial cells (Bonilha et al., 2006; Crepaldi et al., 1997; Saotome et al., 2004), filopodia of neural growth cones (Furutani et al., 2007; Gallo, 2008), or migrating cancer cells (Li et al., 2017; Moodley et al., 2020). On the contrary, ERM deactivation induces a low membrane-cortex attachment, promoting bleb formation in migrating zebrafish progenitors during gastrulation (Diz-Muñoz et al., 2016, 2010; Olguin-Olguin et al., 2021) or during division of drosophila cells (Kunda et al., 2008; Roubinet et al., 2011).

The individual roles of ezrin, radixin, and moesin have been studied without distinction, resulting in a limited understanding of their unique functions within the same cell. To bridge this knowledge gap, we aimed to investigate the specific contributions of each ERM to macrophage migration. Macrophages are innate immune cells that represent the archetype of

the plastic cell capable of infiltrating every tissue of the organism to maintain immune surveillance and tissue homeostasis. Unlike other leukocytes, which rely solely on the protease-independent amoeboid mode of migration (Cougoule et al., 2010; Lämmermann et al., 2008), macrophages adapt their motility strategy to their external environment. In addition to the amoeboid mode, macrophages are capable of infiltrating dense matrices by using a protease-dependent mesenchymal migration that relies on adhesive podosome actin structures (Gui et al., 2018; Van Goethem et al., 2011, 2010). Surprisingly, we found that ERMs are dispensable for macrophages to migrate in diverse contexts, including *in vitro* 2D migration and 3D invasion of extracellular matrix, *ex vivo* tissue infiltration through healthy dermis and tumor tissue, or *in vivo* diapedesis. We further show that neither the thickness nor the mechanics of the actin cortex of macrophage are affected by ERM knock-out.

Results and discussion

The deletion of ezrin, radixin, or moesin does not affect macrophage 3D migration.

In order to investigate the function of ERM proteins in macrophages, we first determined which ERM are expressed in these cells. We confirmed that moesin (Msn) and ezrin (Ezr), but not radixin (Rdx) are expressed in monocytes (Shcherbina et al., 1999). We also showed that all three ERMs are expressed in human blood monocytes derived macrophages (HMDM) (Fig 1A, B). ERMs were also found in macrophages in their phosphorylated, active form (P-ERM), that links the plasma membrane to the actin cytoskeleton (Bretscher et al., 1997; Matsui et al., 1998; Pelaseyed et al., 2017).

We then investigated the localization of ERM proteins in macrophages. For this purpose, we transfected ezrin-, radixin-, and moesin-GFP into human monocyte-derived macrophages (HMDM). All three ERMs localized predominantly at the plasma membrane and decorated membrane ruffles (Fig S1, Movie1-6). Of note, ezrin, but neither radixin nor moesin, was also slightly enriched around podosome cores (Fig S1, A, Movie1, 4). Live observations also revealed that nascent, peripheral, ruffles were enriched in actin filaments, whereas Ezrin, Radixin and Moesin accumulated indifferently on nascent and older, more central, ruffles (Fig S1, D, Movie4-6).

Moesin being described as the most abundant ERM expressed in leukocytes (Shcherbina et al., 1999), we then knocked down the expression of moesin in HMDM using small interfering-RNAs (siRNA). siRNA treatments resulted in an 80% ± 5% moesin depletion (mean ± SD), (Fig 1C). Surprisingly, we found that moesin-depleted human macrophages and wild-type HMDMs exhibited similar levels of infiltration into 3D fibrillar collagen I, an extracellular matrix that promotes the amoeboid mode of motility in macrophages (Van Goethem et al., 2010) (Fig 1D). We also observed that in Matrigel, which promotes protease-dependent mesenchymal

migration of macrophages (Van Goethem et al., 2010), moesin is dispensable for these cells to infiltrate this extracellular matrix (Fig 1E). Yet, a small residual amount of moesin after siRNA may be sufficient to ensure its function. In addition, ezrin and radixin could also potentially replace moesin loss. We therefore decided to knock-out each ERMs using CRISPR-Cas9 gene edition.

We took advantage of an HoxB8-immortalized murine line of macrophage progenitors, which allows an easy and fast generation of progenitors genetically depleted for any gene of interest (Accarias et al., 2020). We first demonstrated that all three ERMs are expressed in mouse HoxB8-macrophages (Fig 1F, G), moesin being the most expressed and phosphorylated ERM (Fig 1F). We first knocked out ezrin, radixin, or moesin individually in hoxB8 progenitors by CRISPR-Cas9. As a control, we used sgRNA targeting the non-expressed luciferase protein, hereafter referred as WT. We achieved a depletion of 89%, 85% and 97% for ezrin, radixin or moesin, respectively, in multiclonal populations of macrophages individually knocked-out for ERMs (Fig 1H). Notably, moesin was the main expressed ERM in macrophages, as evidenced by the lack of detectable western blot signal for ERMs using the pan-ERM antibody in moesin knock-out HoxB8 macrophages. Moreover, among the three ERMs, only moesin knock-out resulted in a significant decrease in P-ERM, suggesting that moesin is also the main activated ERM in HoxB8 macrophages.

Our findings were again unexpected as we discovered that the individual knock-out of any ERM did not affect the 3D migration of macrophages in either collagen I nor in Matrigel (Fig 1I, J). Since the three ERM proteins exhibit high structural similarity and function, it is possible that the other ERMs in each single knock-out compensate for the loss of the knocked-out ERM. To test this hypothesis, we decided to simultaneously knock out all three ERM proteins in HoxB8 macrophage progenitors.

The triple KO of ezrin, radixin, and moesin does not significantly affect the formation and dynamics of actin structures in macrophage.

We generated a triple knockout of the ezrin, radixin and moesin proteins in HoxB8 myeloid progenitors. We isolated three different clonal populations where all three ERM proteins were fully depleted, as validated by immunoblot analysis (Fig 2A), and genomic DNA sequencing (Fig S2), and refer to them as ERM-tKO (clones #1, #2 and #3). To control for potential off-target effects of CRISPR-Cas9 editing, we selected three independent clones that had different genomic mutations in their ezrin, radixin and moesin genes.

As ERMs were found to control the formation and dynamics of diverse actin protrusions (Brown et al., 2003; Furutani et al., 2007; Saotome et al., 2004), we first quantified the formation of these actin structures in ERM-tKO macrophages and progenitors (Fig 2B-G). We observed

that both WT and ERM-TKO progenitors formed a similar number of microvilli-, filopodia- and ruffle-like short protrusions on glass coverslips, as revealed by scanning electron microscopy (SEM) (Fig 2B).

We then found that the ERM-tKO macrophages spread efficiently on bare glass surface in a similar manner than WT macrophages, as demonstrated by their comparable cell area (WT: 916±27 μm^2; TKO: 884±32 μm^2, mean±SEM) and circularity (WT: 0,18±0,007; TKO: 0,19±0,008) compared to the WT (Fig 2D). We also measured that they form the same number of large lamellipodia (Fig 2C), and thin filopodia protrusions (WT: 10,7±1,2 filopodia per cell; TKO: 9,8±1,6), although the latter are slightly longer in the ERM-tKO macrophages (4,9±0,25 µm, mean±SEM, compared to 4,0±0,23 µm in WT macrophages) (Fig 2E). The number of podosomes was also slightly reduced in the ERM-tKO (50±2 podosomes/cell; mean±SEM) compared to WT macrophages (69±3) (Fig 2F), but their dynamics remained unaffected (Fig 2G, Movie 7).

Overall, the absence of ERM proteins in macrophages does not impair the ability of these cells to form the various actin structures involved in migration. Although we observed a slight reduction in the density of podosomes and a slight increase in the length of filopodia, these alterations do not substantially affect the overall formation of actin cortical structures in ERM-deficient macrophages. This contrasts with the microvilli collapse observed in ezrin/moesin double KO in neutrophils and lymphocytes from $Moesin^{Y/-}$ mice (Brown et al., 2003; Hirata et al., 2012; Panicker et al., 2020), and suggests that these small protrusions might not have the same molecular composition in lymphocytes and neutrophils compared to monocyte progenitors.

To investigate whether these modest alterations could affect macrophage migration, we first investigated the ability of ERM-deficient macrophages to migrate randomly on 2D glass, or in response to a gradient of complement 5a (C5a) as a chemoattractant. We found that there were no significant differences in the average velocity (means of WT, 2.6 µm/min; tKO#1, 2.45 µm/min; tKO#2, 2.62 µm/min; tKO#3, 2.36 µm/min) and confinement ratio (WT: 0.20±0.02; tKO#1, 0.14±0.02; tKO#2, 0.18±0.02; tKO#3, 0.19±0.01; mean±SEM) of the 3 ERM-tKO clones and the WT macrophages (Fig 2H and movie 8). ERM-tKO macrophages were also perfectly able to perform chemotaxis toward C5a without any defects in their velocity, directionality or their chemotaxis index (Fig S4 and movie 9).

The 3D infiltration of macrophages *in vitro* remains unaffected by the loss of ezrin, radixin, and moesin.

As macrophage migrate *in vivo* mostly in a tridimensional context we next aimed to test whether ERMs could regulate 3D migration. We previously reported that when invading

collagen I, macrophages rely solely on the protease-independent amoeboid mode of migration while they use protease-dependent mesenchymal migration when they invade Matrigel. We found that ERMs were dispensable for both mode of invasions. All three ERM-tKO clones infiltrated both collagen I (Fig 3A, B) and Matrigel (Fig 3C, D) similarly to WT macrophages. Live imaging of WT and ERM-tKO macrophages in 3D collagen I and Matrigel confirmed that ERM depletion did not affect invasion of macrophages (Movies 10-13). In addition, using live super-resolution imaging of WT and ERM-tKO macrophages stably expressing lifeact-GFP, we found that in 3D collagen, the ruffles formed by tKO macrophages retract at the same rate than WT macrophages, showing that ERMs are not necessary for the dynamics of these actin structures (Fig 3E-H and movies 14 and 15).

Macrophages without ezrin, radixin, and moesin exhibit no impairment in their ability to perform diapedesis and infiltrate the ear derma or fibrosarcoma.

To further investigate the migratory properties of ERM-deficient macrophages *in vivo*, we first assessed their ability to perform diapedesis into mice bearing a fibrosarcoma to induce a major recruitment of monocytes within this tumor (Gui et al., 2018). Indeed, moesin-deficient neutrophils are impaired for diapedesis (Liu et al., 2015; Matsumoto and Hirata, 2016; Panicker et al., 2020).One day differentiated wild-type or ERM-deficient monocyte, were fluorescently labelled with two different cell trackers, mixed in a 1:1 ratio, and co-injected intra-arterially into recipient mice. Using real-time intravital imaging, we assessed the proportion of cells rolling along the tumor vessels and sticking to it. We revealed that the rolling and sticking fractions of ERM-tKO were similar to those of WT macrophages (Fig 4A).

We then demonstrated that ERM are dispensable for the interstitial infiltration of macrophages into various tissues as different as the ear dermis and tumor tissue *ex vivo*. To model interstitial tissue migration, we developed an *ex vivo* migration assay in the mouse ear dermis, in which we allowed differentially labeled WT and ERM-tKO macrophages to infiltrate for three days. To overcome the high heterogeneity of the thin ear tissue, we placed both cell types in the same tissue. Additionally, we switched the cell trackers used to stain the cells between experiments to verify the absence of effects due to staining. Tissue sections followed by immunohistochemistry demonstrated that both tKO and WT macrophages infiltrate the ear derma without any significant difference (Fig 4B). Finally, we evaluated whether ERM-deficient macrophages could infiltrate tumors. As previously described (Accarias et al., 2020; Gui et al., 2018), we generated fibrosarcoma by subcutaneous injection of LPB tumor cells in mice, and the tumors were resected and sliced into thick explants of 500 µm height. A 1:1 mix of cell tracker-labeled WT and tKO-ERM macrophages was seeded on top of the explants, and the infiltration of the macrophages into the tumor tissue was monitored after 3 days. We found that

tKO-ERM macrophages infiltrated the tumor tissue in the same proportion and at the same distance than the WT macrophages (Fig 4C).

ERMs do not control the mechanical properties of the macrophage cortex and are dispensable for Membrane-to-Cortex Attachment (MCA).

Our results demonstrate that ERM proteins, which are recognized for playing crucial roles in the actin cortex (Welf et al., 2020, Lembo et al. 2023), are not required for macrophage migration. We therefore questioned whether ERMs are actually required for the organization of the actin cortex in macrophages by assessing the size and mechanics of these cortexes. Specifically, we used phagocytosis to internalize magnetic beads within WT and tKO-ERM macrophages, and then employed a magnetic field to align the internalized beads with those present in the extracellular environment. By pinching the cortex between the internalized and external beads, we were able to directly measure its thickness and rigidity (Fig 5A-C) (Laplaud et al., 2021). Demonstrating that ERMs are dispensable for the organization of the cortex of macrophages, we did not observe any differences between ERM-tKO and WT macrophages. The thickness of the ERM-tKO cortex (252±29 µm; mean±SEM) was similar those of WT macrophages (284 ±29 µm) (Fig 5D), and when submitted to gradually increasing stresses, we did not measure any differences between the response of the WT (4544 ±662 Pa; mean ±SEM) and ERM-tKO macrophages (6574±1259 Pa) subjected to stresses of gradually increasing intensity (Fig 5E).

Given the absence of structural and mechanical differences in the macrophage cortex upon ERM depletion, we also asked if the physical link between the actomyosin cortex and the plasma membrane (Membrane-to-Cortex Attachment, MCA) is affected. We thus performed dynamic tether pulling using atomic force spectroscopy to quantify MCA in CTL and ERM-TKO HoxB8 macrophage (Fig 5F). In line with the magnetic pinching experiments, we found MCA not to be altered upon ERM depletion (Fig 5G-H). Thus, ERMs seem to be dispensable in macrophages for their canonical function, which is to mechanically link the actomyosin cortex and the plasma membrane.

Finally, to further investigate a functional role of ERM proteins for the dynamic mechanical properties of the macrophage cortex and its attachment to the plasma membrane, we conducted experiments on membrane blebbing. Membrane blebs play an important role in cell migration, particularly in 3D environments, and are promoted by hydrostatic pressure from the cytoplasm that causes cortical actin rupture and plasma membrane protrusions. To retract, blebs require a mechanical link between actomyosin contractions and the plasma membrane of their rim. Interestingly, in all cells studied so far, this mechanical link is strictly dependent on

ERM activity (Charras et al., 2006; Diz-Muñoz et al., 2010; Roubinet et al., 2011). Using time-lapse microscopy to monitor bleb formation, we found that ERMs are unexpectedly dispensable for bleb dynamics in macrophages. We found no significant difference in maximum bleb size and bleb retraction rates between WT and ERM-tKO macrophages (Fig 5I-K and movie 16).

Our study uncovered a surprising finding: ezrin, radixin and moesin are dispensable for key aspects of macrophage behavior, including the formation of lamellipodia and filopodia, the dynamics of membrane ruffles and podosomes, migration *in vitro* (in 2D or 3D matrices) and *ex vivo* (into dermis or tumor tissues) as well as *in vivo* (for macrophage diapedesis). We also demonstrated that ERMs are dispensable for several cortex mechanical properties in macrophages including cortical thickness and stiffness, membrane-to-cortex attachment and control of bleb dynamics. While our wide variety of assays reveal that ERM do not play universal role in cell migration, we cannot entirely rule out that ERMs may be required under specific conditions. In any case, this study challenges the widely held belief that ERMs are universal regulators of cortical organization and cell migration (Akisawa et al., 1999; Arpin et al., 2011; Crepaldi et al., 1997; Louvet-Vallée, 2000; Valderrama et al., 2012). Instead, these findings suggest that the actin cortex of macrophages has evolved to be highly adaptable and plastic, allowing these immune cells to function independently of ERM proteins. This work paves the way for future studies aimed at deciphering the specific functioning of the macrophage cortex.

Methods

Differentiation and culture of human primary monocyte-derived macrophages

Human peripheral blood mononuclear cells were isolated from the blood of healthy donors by centrifugation through Ficoll-Paque Plus (Cytiva), resuspended in cold phosphate buffered saline (PBS) supplemented with 2 mM EDTA, 0.5% heat-inactivated Fetal Calf Serum (FCS) at pH 7.4 and monocytes were magnetically sorted with magnetic microbeads coupled with antibodies directed against CD14 (Miltenyi Biotec #130-050-201). Monocytes were then seeded on glass coverslips at 1.5×10^6 cells/well in six-well plates in RPMI 1640 (Gibco) without FCS. After 2h at 37°C in a humidified 5% CO_2 atmosphere, the medium was replaced by RPMI containing 10% FCS and 20 ng/mL of Macrophage Colony-Stimulating Factor (M-CSF) (Miltenyi 130096489). For experiments, cells were harvested at day 7 using trypsin-EDTA (Fisher Scientific).

RNA interference knockdown

CD14+ human monocytes were transfected with 200 nM siRNA using the HiPerfect system (Qiagen) as described previously. The mix of HiPerfect and siRNA was incubated for 15 min at room temperature and then the cells were added drop by drop. The following siRNA (Dharmacon) were used: human ON-TARGET plus SMART pool siRNA non-targeting control pool (siCtrl) sequence UGGUUUACAUGUCGACUAA; human ON-TARGET plus SMART pool siRNA targeting MSN (moesin) sequences: 5'-CGUAUGCUGUCCAGUCUAA-3'; 5'-GAGGGAAGUUUGGUUCUUU-3'; 5'-UCGCAAGCCUGAUACCAUU-3'; 5'-GGCUGAAACUCAAUAAGAA-3'. After 7 days with siRNAs, macrophages were detached with trypsin-ETDA (Invitrogen) and lysed for western blot analysis or used for 3D collagen and Matrigel migration assays.

Murine HoxB8-progenitors culture and HoxB8-macrophages differentiation

HoxB8 progenitor cells were generated using bone marrow from C57BL/6N Cas9 mice (Tzelepis et al., 2016). Briefly, bone-marrow cells were harvested and hematopoietic progenitor cells were purified by centrifugation using Ficoll-Paque Plus (#17-1440-02). Then, hematopoietic cells were pre-stimulated for 2 days with complete RPMI 1640 medium supplemented with 15% fetal calf serum (FCS), 1% penicillin-streptomycin, 1% glutamine, mouse IL-3, mouse IL-6 and mouse SCF, each at 10 ng/mL (Peprotech). Next, 2×10^5 cells were seeded on a 6-well culture plate in myeloid medium [complete RPMI 1640 medium, supplemented with 20 ng/mL mouse GM-CSF (Miltenyi #130-095-739) and 0.5 µM β-estradiol (Sigma-Aldrich #E2758)] and transduced with 1:5 (vol:vol) Thy1.1-expressing ER-HoxB8

retrovirus supernatant using Lentiblast Premium (OZ Biosciences). After one or two weeks, only ER-HoxB8 immortalized progenitors continue to proliferate. Based on the expression of Thy1.1 marker at the surface of the immortalized progenitors using flow cytometry, we assessed the clean transduction of the progenitor cells. HoxB8 progenitors were then passaged every 2 days in myeloid medium. To differentiate them in macrophages, progenitors were washed twice in PBS to remove estradiol from the medium, and 500,000 cells were plated in 6-well-plate in complete medium containing 20 ng/mL of mM-CSF.

Transfection, transduction, and sequence analysis for the creation of single and triple-knockout in murine HoxB8 progenitors

SgRNAs used for knocking out ERM proteins were EZR: (5'-CTACCCCGAAGACGTGGCCG-3'), RDX: (5'-GCCATCCAGCCCAATACAAC-3'), and MSN: (5'-TATGCCGTCCAGTCTAAGTA-3'). We targeted luciferase as a control, with LUC sgRNA: (5'-GGCGCGGTCGGTAAAGTTGT-3'). For single knockouts, sgRNAs were introduced into pLenti-sgRNA backbone (Addgene #71409) with BsmBI digestion (New Englands Biolabs #R0739) and T4 DNA ligase (Fischer Scientific EL011L). For the triple ERM-knockout, all three sgRNAs were cloned on a same plasmid by golden gate assembly (Kabadi et al., 2014). Briefly, phU6-gRNA (#53188) intermediary plasmid was used to clone EZR gRNA, pmU6-gRNA (#53187) to clone RDX and LUC gRNAs, #53189 ph7SK-gRNA for MSN, and a mock (5'-TTTTTTTTTT-3') sequence was cloned into #53186 phH1-gRNA, and the three plasmids previously mentioned. All intermediary plasmids containing respective sgRNA were then cloned into the final pLV hUbC-Cas9-T2A-GFP plasmid (Addgene #53190), where GFP was replaced by puromycin resistance.

Then, HoxB8 progenitors were knocked-out for ezrin, radixin or moesin using CRISPR Cas9. Briefly, HEK293T cells were co-transfected with pMDL (Addgene #12251), pREV (Addgene #12253), pVSV-G (Addgene #12259) and specific sgRNA-cloned plasmids using Lipofectamine 3000 and OptiMEM according to manufacturer's guidelines to generate lentiviral particles for transduction into Cas9-expressing HoxB8 progenitors. Then, 2×10^5 HoxB8 progenitors were transduced with viral particles and Lentiblast Premium (OZ Biosciences). After 24h, transduced cells were selected with 10 µg/mL of puromycin (Invivogen) for 2 days and validated by immunoblotting. For the triple ERM-KO only, a clonal amplification was performed by single cell sorting and clones were screened for ezrin, radixin and moesin absence of expression by flow cytometry. Immunoblotting with respective ERM antibodies confirmed the depletion of the three ERM proteins in three independent clones (tKO#1, tKO#2, tKO#3). Additionally, total genomic DNA of clonal populations was extracted using TRIzol Reagent (ThermoFisher). Genomic sites encompassing targeted guide regions were amplified

by PCR using GoTaq polymerase (Promega) and sequenced, in order to analyze the genomic point mutations acquired by each clone on the three E, R, M genes.

Western blot

The following rabbit antibodies were purchased from Cell Signaling: anti-ezrin (#3145S, 1/1000), anti-moesin (#3150, 1/1000), anti-radixin (#2636S, 1/1000), anti-pan-ERM (#3142P, WB 1/1000). Rabbit anti-phospho-ERM (1/5000) (Roubinet et al., 2011) and rabbit anti-actin (Sigma-Aldrich A5060, 1/10,000) were also used. Cells were lysed by addition of boiling 2X Laemmli buffer containing phosphatase inhibitors (5 mM sodium orthovanadate, 20 mM sodium fluoride and 25mM β-glycerophosphate). Proteins were subjected to electrophoresis in 8% SDS–PAGE gels, and transferred onto a nitrocellulose membrane. Membranes were saturated with 3% BSA in TBS-T (50 mM Tris, pH 7.2; 150 mM NaCl; and 0.1% Tween 20) for 30 min, and incubated with primary antibodies overnight at 4°C. Then, primary antibodies were revealed using HRP-coupled secondary anti-mouse (Sigma) or anti-rabbit antibodies (Cell Signaling) for 1 h. Finally, HRP activity was revealed using an electrochemiluminescence kit (Amersham) according to the manufacturer's instructions. All quantifications were normalized against actin expression.

In vitro migration assays

2D random migration

2-6×10^3 HoxB8-macrophages were harvested and plated on glass-based 96-wells within complete medium. 2D random migration was recorded every 3 min for 16h with the 10X objective of a wide-field EVOS M7000 (Invitrogen) in an environmental chamber maintaining the temperature at 37°C and 5% CO2. After cell segmentation, tracking of macrophages was done using the automated Trackmate plugin of ImageJ with the LogDetector and Simple LAP tracker. Only the tracks lasting more than 1 hour were kept for the analysis. In addition to the median speed, the confinement ratio was defined as the ratio of the net distance on the total distance traveled by the cell.

2D chemotaxis toward complement 5a (C5a)

25,000 hoxB8-macrophages were seeded in the center part of a µ chemotaxis slide (Ibidi) and let to adhere at 37°C and 5% CO_2 for 10 min. The peripheral chambers were filled with 65 µL of complete medium containing 20 ng/mL murine M-CSF. A C5a gradient (R&D systems #2150C5025) was then generated by adding 30 µL of medium containing 60 nM murine recombinant C5a protein to the left part of the slide. Cells were imaged as in the 2D random

assay every 3 min for 16h. The FastTrackAI artificial Intelligence performed cell tracking, and tracks were filtered using the Chemotaxis and Migration tool (Ibidi, free download from http://www.ibidi.de/applications/ ap_chemo.html).

3D transwell migration in Matrigel and collagen I

For 3D migration assays, 24-transwells (8-µm pores) were loaded with either 100 µl of 10 mg/mL Matrigel™ (Corning) or 110 µl of 2.15 mg/mL fibrillar collagen I (Nutragen), mixed with MEM 10×, H2O, and buffered with bicarbonate solution (Van Goethem et al., 2010). Matrices were allowed to polymerize for 30 min at 37°C, and rehydrated overnight with RPMI 1640 without FCS. The lower chamber was then filled with RPMI 1640 containing 10% FCS and 20 ng/mL mouse M-CSF, and the upper chamber with RPMI 1640 containing 2% FCS and 20 ng/mL mouse M-CSF. 5×10^4 macrophages were serum starved for 3 h and seeded in the upper chamber. Each experiment was performed in triplicate. After 24h, 48h or 72h of migration, z-series of images were acquired at the surface and inside of the matrices with 30 µm intervals. Acquisition and quantification of cell migration was performed using the motorized stage of an inverted video microscope (Leica DMIRB, Leica Microsystems, Deerfield, IL) and the cell counter plugin of the ImageJ software as described previously (Van Goethem et al., 2010). The percentage of migration was obtained after counting the number of cells within the matrix and dividing by the total number of cells. The distribution of the cells into the matrix is represented by plotting the migration distance of each cell.

Ex vivo infiltration of mouse macrophages in tumor and ear derma tissue explants

Ethics:

All experiments on animals were performed according to animal protocols approved by the Animal Care and Use Committee of the Institute of Pharmacology and Structural Biology (APAFIS No. 201609161058531).

Preparation of tumor explants:

1×10^6 LPB fibrosarcoma cell were injected subcutaneously in the flank of C57BL/6 mice to induce a fibrosarcoma (Gui et al., 2018). 1 cm^3 tumors were resected and embedded in 3% low gelling agarose (Sigma-Aldrich #A701) prepared in PBS. 500 µm-thick slices were obtained with the Krumdieck tissue slicer (TSE Systems) filled with ice-cold PBS (Life Technologies) (Gui et al., 2018).

Preparation of ear derma tissue:

Depilated ears from sacrificed C57BL/6 mice were resected. Ear halves were separated under stereomicroscope (Leica microsystems) lengthwise to expose ear derma.

Ex vivo infiltration assays of mouse macrophages in tissue explants:

Tumor slice and ear derma explants were then cultured on a 30-mm cell culture insert featuring a hydrophilic PTFE membrane (0.4 µm pore size, Merck Millipore #PICM0RG50) placed inside 6-well plates containing 1.1 mL of RPMI. A 4 mm diameter stainless-steel washer was then placed on top of each tissue slice to create a well for macrophages seeding. The same day, HoxB8-macrophages CTL and TKO-ERM were differentially labeled with 5 µM Green CellTracker CMFDA (Invitrogen #C7025), or Red CellTracker CMPTX (Invitrogen #C34552) for 30 min at 37°C. Macrophages were harvested and a 1:1 mix of CTL and TKO-ERM macrophages was seeded ($1{,}5\times10^4$ cells / mm²) on top of tissue explants and incubated in a 37°C, 5% CO2 environment for 72 hours. After 16 hours of coculture, the washer was removed. Culture medium (RPMI 1640, Gibco) was replaced daily for 3 days before overnight paraformaldehyde 4% (EMS #15714) tissue fixation at 4°C and embedded in paraffin. The green and red cell trackers were exchanged between experiments in order to verify the absence of effect due to staining.

5 µm-thick ear or tumor paraffin sections were stained with hematoxylin and eosin (HE) or immunostained by immunohistofluorescence. To limit tissue autofluorescence, CMFDA staining of HoxB8 infiltrate in tissue, was stained by anti-fluorescein (1:100, Invitrogen #A889) by overnight incubation at 4°C. The sections were incubated at room temperature with goat anti-rabbit Alexa Fluor 647 (1:200, Invitrogen #A21246) for 2 hours and nuclei were visualized with DAPI (Sigma D9542). The CMPTX cell tracker fluorescence was directly acquired. All images were acquired using a Zeiss Axio Imager M2 using a X20/0.8 Plan Apochromat objective (Zeiss). Images were acquired with an ORCA-flash 4.0 LT (Hamamatsu) camera and processed using Zen software (Zeiss).

For each image, the percentage of infiltrated HoxB8 WT or TKO macrophages, calculated with a threshold of 10 µm under the tissue surface, was compared to the total number of macrophages infiltrated in the tissue. Quantifications were done using ImageJ '*Threshold and Analyze particles'* tool to select CMFDA or CMPTX positive cells, and the measure of migration distance was enabled using the '*Segmented line'* and the '*Straighten*' tools to linearize tissue surface. For ear tissue infiltration, we performed the analysis on 4 ears halves from 4 mice, taking 1-4 sections per ears halves. For analysis of macrophage tumor infiltration, we used 6 *ex vivo* 500µm-slices from 3 tumors, taking 7-9 sections per *ex vivo* slices.

In vivo diapedesis with wide-field intravital microscopy

C57Bl6Jj female mice were subcutaneous injected 100 µL PBS with 5×10^5 MCA Prog (9609) fibrosarcoma tumor cell to induce a fast-growing fibrosarcoma (O'Sullivan et al., 2012). Intravital microscopy was performed at day 8 to 10 before the tumor reach 1 cm^3.

For *in vivo* diapedesis, HoxB8-progenitors were differentiated only for 1 day with 20 ng/mL m-M-CSF. CTL and TKO-ERM so-called HoxB8-monocytes were harvested and differentially labeled with 10 µM Green CellTracker CMFDA (Invitrogen #C7025) and 10 µM Red CellTracker CMPTX (Invitrogen #C34552) for 20 min. Green and red cell trackers were exchanged between experiments. A 1:1 mix of CTL:TKO-ERM cells was resuspended in physiological serum.

Recipient mice were anesthetized by intraperitoneal injection of 1 mg/mL xylazine and 5 mg/mL ketamine per kg/mouse, and placed on a customized stage for securing animals and immobilizing the subcutaneous tumor. A heating pad with temperature feedback to an mTCII micro Temperature Controller (Cell MicroControls, Norflok, VA, USA) was used to maintain the temperature of animals. The right femoral artery was catheterized for retrograde injection of labeled cells, and tumor was exposed for intravital microscopy as previously described (Moussion and Girard, 2011; von Andrian, 1996). Recipient mice were then transferred to a customized intravital video microscopy setup (DM6-FS, Leica Microsystems SAS, Nanterre, France) equipped with water immersion objectives (HCX APO; Leica Microsystems) and an image splitting optics W-VIEW GEMINI (Hamamatsu Photonics, Massy, France) allowing simultaneous image acquisition of dual wavelength images (512/25 and 630/92nm for green and red cell tracker respectively) onto a single camera. Two color fluorescent events in the microcirculation of tumor/draining lymph node were visualized and recorded at 33 frames/seconde by an OrcaFlash LT4.0+ camera and the HCImage software (Hamamatsu Photonics) at multiple positions of the tumor. After combination of green and red images on a single image, rolling fractions, i.e., the percentage of rolling cells in the total flux of cells in each blood vessel; and sticking fractions, i.e., the percentage of rolling cells that firmly adhered for a minimum of 30 seconds, were calculated for all blood vessels imaged in tumor.

Immunofluorescence and cell morphological analysis

For analysis of the morphology of TKO-ERM macrophages, HoxB8-macrophages CTL and TKO-ERM were differentially labeled with 10 µM Blue CellTracker CMAC (Invitrogen #C2110) or 10 µM Red CellTracker CMPTX (Invitrogen #C34552) for 30min. Blue and red cell trackers were exchanged between independent experiments. Macrophages were harvested and a 1:1 mix of CTL and TKO-ERM macrophages were plated on glass coverslips for 1 h. They were fixed for 10 min in 3.7% paraformaldehyde solution containing 15 mM sucrose in Phosphate Buffer Saline (PBS) (Fisher Scientific) at room temperature. After fixation, cells were

permeabilized for 10 min with PBS/0.3% Triton and blocked with PBS/0.3% Triton/1% BSA. Samples were incubated with green AlexaFluor 488-conjugated phalloidin (Invitrogen) for 30min, then washed and mounted. Mosaic images were acquired using a Zeiss Axio Imager M2 using a X100/1,4 Plan Apochromat objective (Zeiss). Cells were semi-automatically segmented to measure their area and circularity based on their actin staining. WT and TKO ERM cells were differentiated based on their respective cell tracker, which were inversed between experiments to ensure they do not have an effect. Then, podosomes were detected using the 'Find Maxima' function of the ImageJ software. Filopodia of 30 cells for each condition were manually traced to get their length and number per cell.

Live structural illumination microscopy (SIM) imaging of ezrin, radixin, and moesin transfected in human macrophages

For live imaging of ERM proteins shown in Movies 1-6, primary human macrophages were detached using trypsin-EDTA and transfected with Lifeact-mCherry and either ezrin-GFP, radixin-GFP or moesin-GFP plasmids 4h before observation using a Neon® MP5000 electroporation system (Invitrogen) with the following parameters: two 1000V, 40 ms pulses, with 0.5 µg DNA each for 2×10^5 cells. Ezrin-GFP from Leguay et al., 2021, Radixin-GFP and Moesin–GFP were obtained by subcloning PCR amplified Ezrin, Radixin and Moesin, respectively, into pEGFP-N1 vector (Clontech). All PCRs were performed using Phusion High-Fidelity DNA Polymerase (New England Biolabs).

SIM live images of double-transfected cells were acquired every 15 s using a Plan-Apochromat 63x/1.4 Oil DIC M27 on an Elyra 7 microscope (Zeiss) and 129 nm-interspaced Z-stacks were also acquired. Super-resolution reconstruction was done with Zen Black (3.0 SR) SIM algorithm 3D leap processing with autosharpess. Chromatic aberrations were corrected with a channel alignment calculated from a multicolor subresolutive beads acquisition from the same half-day.

Scanning Electron microscopy

HoxB8 progenitors and macrophages were fixed using 0.1 M sodium cacodylate buffer (pH 7.4) supplemented with 2.5% (v/v) glutaraldehyde. After post-fixation in 1% osmium tetraoxide (in 0.2 mol/L cacodylate buffer), cells were dehydrated in a series of increasing ethanol concentrations and critical point dried using carbon dioxide. After coating with gold, cells were examined with a JEOL JSM-6700F scanning electron microscope. For image analysis, protrusions of each HoxB8-progenitor cells present in a square of $4\mu m^2$ were manually counted. Lamellipodia of HoxB8-macrophages were manually detoured and expressed as a percentage of the cell perimeter.

Live random illumination microscopy of actin structures

For live imaging of the actin remodeling in 2D and 3D matrices, shown in Movies 7, 14 and 15, HoxB8-WT and ERM-TKO (tKO#1) progenitors were stably transduced with Lifeact-GFP plasmid-containing virus. Cells were sorted by flow cytometry according to their GFP expression. Subsequent differentiated macrophages were detached using PBS-EDTA and plated on Ibidi wells (8 wells Ibidi #80826), either directly in 2D bare glass, or mixed with 100% Matrigel, or 2,15 mg/mL collagen I at 2×10^6 cells per mL, and allowed to polymerize for 30 min in the incubator before adding complete medium. Random Illumination Microscopy was then performed using a home-made system (Mangeat et al., 2021). Images were acquired every 10 s for 5 min using an inverted microscope (TEi Nikon) equipped with a 100x magnification, 1.49 N.A. objective (CFI SR APO 100XH ON 1.49 NIKON) and an sCMOS camera (ORCA-Flash4.0 LT, Hamamatsu). Fast diode lasers (Oxxius) with respective wavelengths 488 nm (LBX-488-200-CSB) and 561 nm (LMX-561L-200-COL) were collimated using a fiber collimator (RGBV Fiber Collimators 60FC Sukhamburg) to produce TEM00 2.2 mm-diameter beam. The polarization beam was rotated with an angle of 5 degrees before hitting a X4 Beam Expander beam (GBE04-A) and produced a 8.8 mm TEM00 beam. A fast spatial light phase binary modulator (QXGA fourth dimensions) was conjugated to the image plane to create speckle random illumination. Image reconstruction was then performed as detailed in (Mangeat et al., 2021) and at https://github.com/teamRIM/tutoRIM.

Analysis of podosome maintenance in 2D was performed using ImageJ. Briefly, we quantified the number of podosomes appearing, maintained, or disappearing between 4 images at 1-minute intervals (Fig S3). Analysis of ruffle retraction in 3D collagen I was performed as follow. The ruffle dynamics were analyzed in videos of 300 s with a 10 s frequency: using ImageJ, we measured the length of the protrusion at its maximal elongation, and the time until the protrusion disappeared.

Measure of cortex thickness and dynamics

Beads preparation

Superparamegnetic microbeads M-450 (Dynabeads) were prepared in two solutions. For both, 60 µL of stock solution was washed three times with PBS using a magnet to retain the beads in the pellet between each rinsing. They were then re-suspended in 200 µL of complete medium (DMEM + 10% FBS) for the bead solution n°1, and in 200 µL of 0.5 mg/mL PLL-g-PEG (Peg 2 kDa, SuSos) in HEPES for the bead solution n°2. Both were placed on a wheel for 8h to get coated by their respective medium. In the following methods, beads from the first solution were incubated with cells to be ingested, while those from the second solution were

intended to be less likely intaken.

Magnetic setup

As described in (Laplaud et al., 2021), an Axio A1 inverted microscope (Carl Zeiss, Germany) is used as the base for the Magnetic Pincher setup. Imaged are produced using an oil-immersion 100× objective [1.4 numerical aperture] mounted on a piezo-controlled translator (Physik Instrumente) and recorded with an Orca Flash4 camera (Hamamatsu Photonics). Two coaxial coils (SBEA) with mu metal core (length, 40 mm; diameter, 26 to 88 mm; 750 spires) are placed in Helmoltz configuration in a way to generate a quasi-homogeneous magnetic field in the sample region. They are powered by a bipolar operational power supply amplifier 6A/36V (Kepco) controlled by a data acquisition module (National Instruments). The maximum field generated is 54mT with a gradient less than 0.1 $mT \cdot mm^{-1}$ over the sample. During an experiment, the self-organization of beads is first triggered with a constant field of 5mT before acquisition of time-lapse images. The sample is maintained at 37°C using the Box and the Cube from Life Imaging Systems. The setup is controlled via a data acquisition module by a custom LabVIEW interface that ensures the synchronicity between piezo position, magnetic field imposition, and image acquisition.

Pinching experiment

CTL and ERM-TKO HoxB8 macrophages were plated on glass in Petri dishes and in each of them 1 µL of the bead solution n°1 was added ($1{,}5\times10^5$ beads) and incubated for 30min so that the cells would take up the beads. Then 2 µL of bead solution n°2 was added and the medium was supplemented with 20 mM HEPES buffer, to maintain the pH of the medium during the experiment without CO_2 control. For each dish, cells with their cortex pinched between beads were imaged with the previously described magnetic setup. In each film acquisition, the nominal magnetic field exerted by the coils was 5 mT (100pN), every 10s the field was lowered to 1 mT (31 pN), then increased to 54 mT (1150 pN) in 1.5 s, and then brought back to 5 mT (values between brackets are the corresponding typical force values). This series of compression-relaxation was repeated 6 to 10 times per cell, and an epifluorescence image of the LifeAct-GFP signal was taken between each cycle. In addition to the images, the precise time and magnetic field corresponding to each image was recorded.

Data analysis

Using Fiji's plugin "Analyze Particle", the center of all beads on each image of time-lapse was detected with a subpixel resolution (Laplaud et al., 2021). Using a home-made tracking

algorithm written in Python (https://github.com/jvermeil-biophys/CortExplore_PublicVersion) the trajectories in 3D of the centers of the two beads pinching the cortex were detected, and the thickness of the pinched cortex was computed. The pinching force was also computed knowing the distance between the beads, the external magnetic field and the magnetization function of the beads. This analysis was complemented by a visual inspection of the LifeAct-GFP images of the cells and compressions occurring while a phagocytosis process had begun were removed from the dataset.

To characterize the cortex thickness, the metric we chose is the median of the cortical thickness at 5 mT (nominal field), which corresponds to a typical force of 100+/-18 pN.

To compute the elastic modulus at low stress, we computed the strain-stress curve corresponding to each compression using a model developed by R. S. Chadwick for this specific geometry (Chadwick, 2002). Then we fitted the slope of these strain-stress curves between 150 and 350Pa.

Atomic force spectroscopy

CTL and ERM-TKO HoxB8 macrophages were plated into a 35mm Fluorodish (WPI) 24h before the experiment. 30min prior to the AFM experiment, the serum concentration in the medium was reduced to 2% FBS.

qp-SCONT cantilevers (Nanosensors) were mounted on a CellHesion 200 AFM (Bruker), connected into an Eclipse Ti inverted light microscope (Nikon). Cantilevers were calibrated using the contact-based approach, followed by coating with 4 mg/ml Concanavalin A (Sigma) for 1 hour at 37°C. Cantilevers were washed with 1x PBS before the measurements. MCA (Membrane-to-Cortex Attachment) was estimated using dynamic tether pulling as follows: Approach velocity was set to 0.5 µm/s, with a contact force of 200 pN, and contact time was varied between 100 ms to 10 s, aiming at maximizing the probability to extrude single tethers. The cantilever was then retracted for 80 µm at a velocity of 2, 5, 10 or 30 µm/s. Tether force at the moment of tether breakage was recorded at a sampling rate of 2000 Hz. Resulting force curves were analyzed using the JPK Data Processing Software and the resulting force-velocity data was fitted to the Brochard-Wyart model (Brochard-Wyart et al., 2006) to allow estimation of an MCA parameter Alpha, that is proportional to the density of binders (i.e. the active MCA molecules) and the emerging effective viscosity. Measurements were run at 37 C with 5% CO2 and samples were used no longer than 1 h for data acquisition. More details on the method can be found in (Bergert and Diz-Muñoz, 2023).

Statistical analysis

Statistical analysis was done using GraphPad Prism 9.0 (GraphPad Software Inc.). For western blot quantifications, the expression of each protein in human or HoxB8 macrophages was compared to monocytes or Hox progenitors, two by two, respectively, using a ratio paired two-tailed t-test. For all migration experiments including 3D migration percentage, distance, and the velocity, directionality, FMIx and confinement ratio of 2D migrations; the means of each 3 independent experiments was compared to WT condition using either paired t-test for comparison of 2 conditions, or RM Anova one-way for more than 2 conditions.

For morphological experiments based on SEM, and actin immunofluorescence analysis, data were compared between TKO cells and control cells using the two-tailed Mann-Whitney test. In all cases * correspond to $p < 0.05$.

Acknowledgements

This work benefited from the assistance of Isabelle Fourqueaux (CMEAB), Emmanuelle Naser and Eve Pitot (IPBS) from the imaging and cytometry facility TRI, member of the national infrastructure France-BioImaging infrastructure supported by the French National Research Agency and Etienne Meunier for providing access to wide-field EVOS microscope. The authors thank Tim Lammermann, Paul Mangeat, Eva Kiermaier, Emmanuelle Planus, Pablo Vargas, Christel Lutz, François Payre and Damien Ramel for helpful discussions. This work was supported by the Université Toulouse III - Paul Sabatier (UT3), ITMO Cancer of Aviesan on funds managed by Inserm (RP), the CIHR (PJT162109) (SC), Globalink-MITACS (PV), l'Agence Nationale de la Recherche (ANR-21-CE13-0048) and the Institut Pierre-Gilles de Gennes-IPGG (Equipement d'Excellence, "Investissements d'avenir," program ANR-10-EQPX-34 and Laboratoire d'Excellence, "Investissements d'avenir" program ANR-10-IDEX-0001-02 PSL and ANR-10-LABX-31) (JV and ODR) and the European Molecular Biology Laboratory (EMBL) (MB and ADM).

References

Accarias, S., Sanchez, T., Labrousse, A., Ben-Neji, M., Boyance, A., Poincloux, R., Maridonneau-Parini, I., Le Cabec, V., 2020. Genetic engineering of hoxb8 immortalized hematopoietic progenitors: a potent tool to study macrophage tissue migration. Journal of Cell Science 133, jcs236703. https://doi.org/10.1242/jcs.236703

Akisawa, N., Nishimori, I., Iwamura, T., Onishi, S., Hollingsworth, M.A., 1999. High levels of ezrin expressed by human pancreatic adenocarcinoma cell lines with high metastatic potential. Biochem. Biophys. Res. Commun. 258, 395–400. https://doi.org/10.1006/bbrc.1999.0653

Baeyens, N., Latrache, I., Yerna, X., Noppe, G., Horman, S., Morel, N., 2013. Redundant control of migration and adhesion by ERM proteins in vascular smooth muscle cells. Biochem. Biophys. Res. Commun. 441, 579–585. https://doi.org/10.1016/j.bbrc.2013.10.118

Barger, S.R., Reilly, N.S., Shutova, M.S., Li, Q., Maiuri, P., Heddleston, J.M., Mooseker, M.S., Flavell, R.A., Svitkina, T., Oakes, P.W., Krendel, M., Gauthier, N.C., 2019. Membrane-cytoskeletal crosstalk mediated by myosin-I regulates adhesion turnover during phagocytosis. Nat Commun 10, 1249. https://doi.org/10.1038/s41467-019-09104-1

Bergert, M., Diz-Munoz, A., 2023. Quantification of Apparent Membrane Tension and Membrane-to-Cortex attachment in Animal Cells Using Atomic Force Microscopy-Based Force Spectroscopy. Methods Mol Biol, 2600:45-62. https://doi.org/10.1007/978-1-0716-2851-5_3

Bonilha, V.L., Rayborn, M.E., Saotome, I., McClatchey, A.I., Hollyfield, J.G., 2006. Microvilli defects in retinas of ezrin knockout mice. Experimental Eye Research 82, 720–729. https://doi.org/10.1016/j.exer.2005.09.013

Bretscher, A., 1983. Purification of an 80,000-dalton protein that is a component of the isolated microvillus cytoskeleton, and its localization in nonmuscle cells. Journal of Cell Biology 97, 425–432. https://doi.org/10.1083/jcb.97.2.425

Bretscher, A., Reczek, D., Berryman, M., 1997. Ezrin: a protein requiring conformational activation to link microfilaments to the plasma membrane in the assembly of cell surface structures. Journal of Cell Science 110, 3011–3018. https://doi.org/10.1242/jcs.110.24.3011

Brochard-Wyart, F., Borghi, N., Cuvelier, D., Nassoy, P., 2006. Hydrodynamic narrowing of tubes extruded from cells. Proc Natl Acad Sci U S A 103(20):7660–7663 https://doi.org/10.1073/pnas.0602012103

Brown, M.J., Nijhara, R., Hallam, J.A., Gignac, M., Yamada, K.M., Erlandsen, S.L., Delon, J., Kruhlak, M., Shaw, S., 2003. Chemokine stimulation of human peripheral blood T lymphocytes induces rapid dephosphorylation of ERM proteins, which facilitates loss of microvilli and polarization. Blood 102, 3890–3899. https://doi.org/10.1182/blood-2002-12-3807

Carreno, S., Kouranti, I., Glusman, E.S., Fuller, M.T., Echard, A., Payre, F., 2008. Moesin and its activating kinase Slik are required for cortical stability and microtubule organization in mitotic cells. J. Cell Biol. 180, 739–746. https://doi.org/10.1083/jcb.200709161

Chadwick, R.S., 2002. Axisymmetric Indentation of a Thin Incompressible Elastic Layer. SIAM Journal on Applied Mathematics 62, 1520–1530.

Chugh, P., Paluch, E.K., 2018. The actin cortex at a glance. Journal of Cell Science 131, jcs186254. https://doi.org/10.1242/jcs.186254

Cougoule, C., Le Cabec, V., Poincloux, R., Al Saati, T., Mège, J.-L., Tabouret, G., Lowell, C.A., Laviolette-Malirat, N., Maridonneau-Parini, I., 2010. Three-dimensional migration of macrophages requires Hck for podosome organization and extracellular matrix proteolysis. Blood 115, 1444–1452. https://doi.org/10.1182/blood-2009-04-218735

Cougoule, C., Van Goethem, E., Le Cabec, V., Lafouresse, F., Dupré, L., Mehraj, V., Mège, J.-L., Lastrucci, C., Maridonneau-Parini, I., 2012. Blood leukocytes and macrophages of various phenotypes have distinct abilities to form podosomes and to migrate in 3D environments. European Journal of Cell Biology, Podosomes, Invadopodia and Focal Adhesions in Physiology and Pathology 91, 938–949. https://doi.org/10.1016/j.ejcb.2012.07.002

Crepaldi, T., Gautreau, A., Comoglio, P.M., Louvard, D., Arpin, M., 1997. Ezrin is an effector of hepatocyte growth factor-mediated migration and morphogenesis in epithelial cells. J. Cell Biol. 138, 423–434. https://doi.org/10.1083/jcb.138.2.423

Diz-Muñoz, A., Krieg, M., Bergert, M., Ibarlucea-Benitez, I., Muller, D.J., Paluch, E., Heisenberg, C.-P., 2010. Control of Directed Cell Migration In Vivo by Membrane-to-Cortex Attachment. PLoS Biol 8, e1000544. https://doi.org/10.1371/journal.pbio.1000544

Diz-Muñoz, A., Romanczuk, P., Yu, W., Bergert, M., Ivanovitch, K., Salbreux, G., Heisenberg, C.-P., Paluch, E.K., 2016. Steering cell migration by alternating blebs and actin-rich protrusions. BMC Biology 14, 74. https://doi.org/10.1186/s12915-016-0294-x

Furutani, Y., Matsuno, H., Kawasaki, M., Sasaki, T., Mori, K., Yoshihara, Y., 2007. Interaction between Telencephalin and ERM Family Proteins Mediates Dendritic Filopodia Formation. J. Neurosci. 27, 8866–8876. https://doi.org/10.1523/JNEUROSCI.1047-07.2007

Gallo, G., 2008. Semaphorin 3A inhibits ERM protein phosphorylation in growth cone filopodia through inactivation of PI3K. Developmental Neurobiology 68, 926–933. https://doi.org/10.1002/dneu.20631

Gui, P., Ben-Neji, M., Belozertseva, E., Dalenc, F., Franchet, C., Gilhodes, J., Labrousse, A., Bellard, E., Golzio, M., Poincloux, R., Maridonneau-Parini, I., Le Cabec, V., 2018. The Protease-Dependent Mesenchymal Migration of Tumor-Associated Macrophages as a Target in Cancer Immunotherapy. Cancer Immunol Res 6, 1337–1351. https://doi.org/10.1158/2326-6066.CIR-17-0746

Gupta, P., Gauthier, N.C., Cheng-Han, Y., Zuanning, Y., Pontes, B., Ohmstede, M., Martin, R., Knölker, H.-J., Döbereiner, H.-G., Krendel, M., Sheetz, M., 2013. Myosin 1E localizes to actin polymerization sites in lamellipodia, affecting actin dynamics and adhesion formation. Biology Open 2, 1288–1299. https://doi.org/10.1242/bio.20135827

Hirata, T., Nomachi, A., Tohya, K., Miyasaka, M., Tsukita, S., Watanabe, T., Narumiya, S., 2012. Moesin-deficient mice reveal a non-redundant role for moesin in lymphocyte homeostasis. International Immunology 24, 705–717. https://doi.org/10.1093/intimm/dxs077

Kunda, P., Rodrigues, N.T.L., Moeendarbary, E., Liu, T., Ivetic, A., Charras, G., Baum, B., 2012. PP1-Mediated Moesin Dephosphorylation Couples Polar Relaxation to Mitotic Exit. Current Biology 22, 231–236. https://doi.org/10.1016/j.cub.2011.12.016

Lämmermann, T., Bader, B.L., Monkley, S.J., Worbs, T., Wedlich-Söldner, R., Hirsch, K., Keller, M., Förster, R., Critchley, D.R., Fässler, R., Sixt, M., 2008. Rapid leukocyte migration by integrin-independent flowing and squeezing. Nature 453, 51–55. https://doi.org/10.1038/nature06887

Lan, S., Zheng, X., Hu, P., Xing, X., Ke, K., Wang, F., Cheng, N., Zhuang, Q., Liu, X., Liu, J., Zhao, B., Wang, Y., 2020. Moesin facilitates metastasis of hepatocellular carcinoma cells by improving invadopodia formation and activating β-catenin/MMP9 axis. Biochemical and Biophysical Research Communications 524, 861–868. https://doi.org/10.1016/j.bbrc.2020.01.157

Lankes, W.T., Furthmayr, H., 1991. Moesin: a member of the protein 4.1-talin-ezrin family of proteins. Proceedings of the National Academy of Sciences 88, 8297–8301. https://doi.org/10.1073/pnas.88.19.8297

Laplaud, V., Levernier, N., Pineau, J., Roman, M.S., Barbier, L., Sáez, P.J., Lennon-Duménil, A.-M., Vargas, P., Kruse, K., du Roure, O., Piel, M., Heuvingh, J., 2021. Pinching the cortex of live cells reveals thickness instabilities caused by myosin II motors. Science Advances 7, eabe3640. https://doi.org/10.1126/sciadv.abe3640

Larson, S.M., Lee, H.J., Hung, P., Matthews, L.M., Robinson, D.N., Evans, J.P., 2010. Cortical Mechanics and Meiosis II Completion in Mammalian Oocytes Are Mediated by Myosin-II and Ezrin-Radixin-Moesin (ERM) Proteins. MBoC 21, 3182–3192. https://doi.org/10.1091/mbc.e10-01-0066

Leguay, K., Decelle, B., He, Y.Y., Pagniez, A., Hogue, M., Kobayashi, H., Le Gouill, C., Bouvier, M., Carréno, S., 2021. Development of conformational BRET biosensors that monitor ezrin, radixin and moesin activation in real time. J Cell Sci 134, jcs255307. https://doi.org/10.1242/jcs.255307

Lembo, S., Strauss, L., Cheng, D., Vermeil, J., Siggel, M., Toro-Nahuelpan, M., Chan, C.J., Kosinski, J., Piel, M., Du Roure, O., Heuvingh, J., Mahamid, J., Diz-Muñoz, A., 2023. The distance between the plasma membrane and the actomyosin cortex acts as a nanogate to control cell surface mechanics. bioRxiv 2023.01.31.526409. https://doi.org/10.1101/2023.01.31.526409

Li, L.-Y., Xie, Y.-H., Xie, Y.-M., Liao, L.-D., Xu, X.-E., Zhang, Q., Zeng, F.-M., Tao, L.-H., Xie, W.-M., Xie, J.-J., Xu, L.-Y., Li, E.-M., 2017. Ezrin Ser66 phosphorylation regulates invasion and metastasis of esophageal squamous cell carcinoma cells by mediating filopodia formation. The International Journal of Biochemistry & Cell Biology 88, 162–171. https://doi.org/10.1016/j.biocel.2017.05.018

Liu, X., Yang, T., Suzuki, K., Tsukita, S., Ishii, M., Zhou, S., Wang, G., Cao, L., Qian, F., Taylor, S., Oh, M.-J., Levitan, I., Ye, R.D., Carnegie, G.K., Zhao, Y., Malik, A.B., Xu, J., 2015. Moesin and myosin phosphatase confine neutrophil orientation in a chemotactic gradient. J. Exp. Med. 212, 267–280. https://doi.org/10.1084/jem.20140508

Liu, Y., Belkina, N.V., Park, C., Nambiar, R., Loughhead, S.M., Patino-Lopez, G., Ben-Aissa, K., Hao, J.-J., Kruhlak, M.J., Qi, H., von Andrian, U.H., Kehrl, J.H., Tyska, M.J., Shaw, S., 2012. Constitutively active ezrin increases membrane tension, slows migration, and impedes endothelial transmigration of lymphocytes in vivo in mice. Blood 119, 445–453. https://doi.org/10.1182/blood-2011-07-368860

Louvet-Vallée, S., 2000. ERM proteins: From cellular architecture to cell signaling. Biology of the Cell 92, 305–316. https://doi.org/10.1016/S0248-4900(00)01078-9

Mangeat, T., Labouesse, S., Allain, M., Negash, A., Martin, E., Guénolé, A., Poincloux, R., Estibal, C., Bouissou, A., Cantaloube, S., Vega, E., Li, T., Rouvière, C., Allart, S., Keller, D., Debarnot, V., Wang, X.B., Michaux, G., Pinot, M., Le Borgne, R., Tournier, S., Suzanne, M.,

Idier, J., Sentenac, A., 2021. Super-resolved live-cell imaging using random illumination microscopy. Cell Rep Methods 1, 100009. https://doi.org/10.1016/j.crmeth.2021.100009

Matsui, T., Maeda, M., Doi, Y., Yonemura, S., Amano, M., Kaibuchi, K., Tsukita, S., Tsukita, S., 1998. Rho-kinase phosphorylates COOH-terminal threonines of ezrin/radixin/moesin (ERM) proteins and regulates their head-to-tail association. J. Cell Biol. 140, 647–657. https://doi.org/10.1083/jcb.140.3.647

Matsumoto, M., Hirata, T., 2016. Moesin regulates neutrophil rolling velocity in vivo. Cellular Immunology 304–305, 59–62. https://doi.org/10.1016/j.cellimm.2016.04.007

Mazerik, J.N., Kraft, L.J., Kenworthy, A.K., Tyska, M.J., 2014. Motor and tail homology 1 (Th1) domains antagonistically control myosin-1 dynamics. Biophys J 106, 649–658. https://doi.org/10.1016/j.bpj.2013.12.038

McClatchey, A.I., 2014. ERM proteins at a glance. J. Cell. Sci. 127, 3199–3204. https://doi.org/10.1242/jcs.098343

Moodley, S., Lian, E.Y., Crupi, M.J.F., Hyndman, B.D., Mulligan, L.M., 2020. RET isoform-specific interaction with scaffold protein Ezrin promotes cell migration and chemotaxis in lung adenocarcinoma. Lung Cancer 142, 123–131. https://doi.org/10.1016/j.lungcan.2020.02.004

Moussion, C., Girard, J.-P., 2011. Dendritic cells control lymphocyte entry to lymph nodes through high endothelial venules. Nature 479, 542–546. https://doi.org/10.1038/nature10540

Navinés-Ferrer, A., Martín, M., 2020. Long-Tailed Unconventional Class I Myosins in Health and Disease. Int J Mol Sci 21, 2555. https://doi.org/10.3390/ijms21072555

Niggli, V., Rossy, J., 2008. Ezrin/radixin/moesin: Versatile controllers of signaling molecules and of the cortical cytoskeleton. The International Journal of Biochemistry & Cell Biology 40, 344–349. https://doi.org/10.1016/j.biocel.2007.02.012

Olguin-Olguin, A., Aalto, A., Maugis, B., Boquet-Pujadas, A., Hoffmann, D., Ermlich, L., Betz, T., Gov, N.S., Reichman-Fried, M., Raz, E., 2021. Chemokine-biased robust self-organizing polarization of migrating cells in vivo. Proceedings of the National Academy of Sciences 118, e2018480118. https://doi.org/10.1073/pnas.2018480118

O'Sullivan, T., Saddawi-Konefka, R., Vermi, W., Koebel, C.M., Arthur, C., White, J.M., Uppaluri, R., Andrews, D.M., Ngiow, S.F., Teng, M.W.L., Smyth, M.J., Schreiber, R.D., Bui, J.D., 2012. Cancer immunoediting by the innate immune system in the absence of adaptive immunity. J Exp Med 209, 1869–1882. https://doi.org/10.1084/jem.20112738

Panicker, S.R., Yago, T., Shao, B., McEver, R.P., 2020. Neutrophils lacking ERM proteins polarize and crawl directionally but have decreased adhesion strength. Blood Advances 4, 3559–3571. https://doi.org/10.1182/bloodadvances.2020002423

Pelaseyed, T., Viswanatha, R., Sauvanet, C., Filter, J.J., Goldberg, M.L., Bretscher, A., 2017. Ezrin activation by LOK phosphorylation involves a PIP2-dependent wedge mechanism. Elife 6, e22759. https://doi.org/10.7554/eLife.22759

Roch, F., Polesello, C., Roubinet, C., Martin, M., Roy, C., Valenti, P., Carreno, S., Mangeat, P., Payre, F., 2010. Differential roles of PtdIns(4,5)P2 and phosphorylation in moesin activation during Drosophila development. J Cell Sci 123, 2058–2067. https://doi.org/10.1242/jcs.064550

Roubinet, C., Decelle, B., Chicanne, G., Dorn, J.F., Payrastre, B., Payre, F., Carreno, S., 2011. Molecular networks linked by Moesin drive remodeling of the cell cortex during mitosis. J Cell Biol 195, 99–112. https://doi.org/10.1083/jcb.201106048

Rouven Brückner, B., Pietuch, A., Nehls, S., Rother, J., Janshoff, A., 2015. Ezrin is a Major Regulator of Membrane Tension in Epithelial Cells. Sci Rep 5, 14700. https://doi.org/10.1038/srep14700

Saotome, I., Curto, M., McClatchey, A.I., 2004. Ezrin Is Essential for Epithelial Organization and Villus Morphogenesis in the Developing Intestine. Developmental Cell 6, 855–864. https://doi.org/10.1016/j.devcel.2004.05.007

Shcherbina, A., Bretscher, A., Kenney, D.M., Remold-O'Donnell, E., 1999. Moesin, the major ERM protein of lymphocytes and platelets, differs from ezrin in its insensitivity to calpain. FEBS Letters 443, 31–36. https://doi.org/10.1016/S0014-5793(98)01674-3

Tsujita, K., Satow, R., Asada, S., Nakamura, Y., Arnes, L., Sako, K., Fujita, Y., Fukami, K., Itoh, T., 2021. Homeostatic membrane tension constrains cancer cell dissemination by counteracting BAR protein assembly. Nat Commun 12, 5930. https://doi.org/10.1038/s41467-021-26156-4

Tsukita, S., Hieda, Y., Tsukita, S., 1989. A new 82-kD barbed end-capping protein (radixin) localized in the cell-to-cell adherens junction: purification and characterization. J Cell Biol 108, 2369–2382. https://doi.org/10.1083/jcb.108.6.2369

Tyska, M.J., Mackey, A.T., Huang, J.-D., Copeland, N.G., Jenkins, N.A., Mooseker, M.S., 2005. Myosin-1a is critical for normal brush border structure and composition. Mol Biol Cell 16, 2443–2457. https://doi.org/10.1091/mbc.e04-12-1116

Tzelepis, K., Koike-Yusa, H., De Braekeleer, E., Li, Y., Metzakopian, E., Dovey, O.M., Mupo, A., Grinkevich, V., Li, M., Mazan, M., Gozdecka, M., Ohnishi, S., Cooper, J., Patel, M., McKerrell, T., Chen, B., Domingues, A.F., Gallipoli, P., Teichmann, S., Ponstingl, H., McDermott, U., Saez-Rodriguez, J., Huntly, B.J.P., Iorio, F., Pina, C., Vassiliou, G.S., Yusa, K., 2016. A CRISPR Dropout Screen Identifies Genetic Vulnerabilities and Therapeutic Targets in Acute Myeloid Leukemia. Cell Reports 17, 1193–1205. https://doi.org/10.1016/j.celrep.2016.09.079

Valderrama, F., Thevapala, S., Ridley, A.J., 2012. Radixin regulates cell migration and cell-cell adhesion through Rac1. J. Cell. Sci. 125, 3310–3319. https://doi.org/10.1242/jcs.094383

Van Goethem, E., Guiet, R., Balor, S., Charrière, G.M., Poincloux, R., Labrousse, A., Maridonneau-Parini, I., Le Cabec, V., 2011. Macrophage podosomes go 3D. European Journal of Cell Biology, Invadosomes 90, 224–236. https://doi.org/10.1016/j.ejcb.2010.07.011

Van Goethem, E., Poincloux, R., Gauffre, F., Maridonneau-Parini, I., Le Cabec, V., 2010. Matrix architecture dictates three-dimensional migration modes of human macrophages: differential involvement of proteases and podosome-like structures. J Immunol 184, 1049–1061. https://doi.org/10.4049/jimmunol.0902223

von Andrian, U.H., 1996. Intravital microscopy of the peripheral lymph node microcirculation in mice. Microcirculation 3, 287–300. https://doi.org/10.3109/10739689609148303

Vorselen, D., Barger, S.R., Wang, Y., Cai, W., Theriot, J.A., Gauthier, N.C., Krendel, M., 2021. Phagocytic 'teeth' and myosin-II 'jaw' power target constriction during phagocytosis. eLife 10, e68627. https://doi.org/10.7554/eLife.68627

Welf, E.S., Miles, C.E., Huh, J., Sapoznik, E., Chi, J., Driscoll, M.K., Isogai, T., Noh, J., Weems, A.D., Pohlkamp, T., Dean, K., Fiolka, R., Mogilner, A., Danuser, G., 2020. Actin-Membrane Release Initiates Cell Protrusions. Developmental Cell 55, 723-736.e8. https://doi.org/10.1016/j.devcel.2020.11.024

Xu, J., Zhang, W., 2021. EZR promotes pancreatic cancer proliferation and metastasis by activating FAK/AKT signaling pathway. Cancer Cell Int 21, 1–15. https://doi.org/10.1186/s12935-021-02222-1

Verdys et al. Figure 1

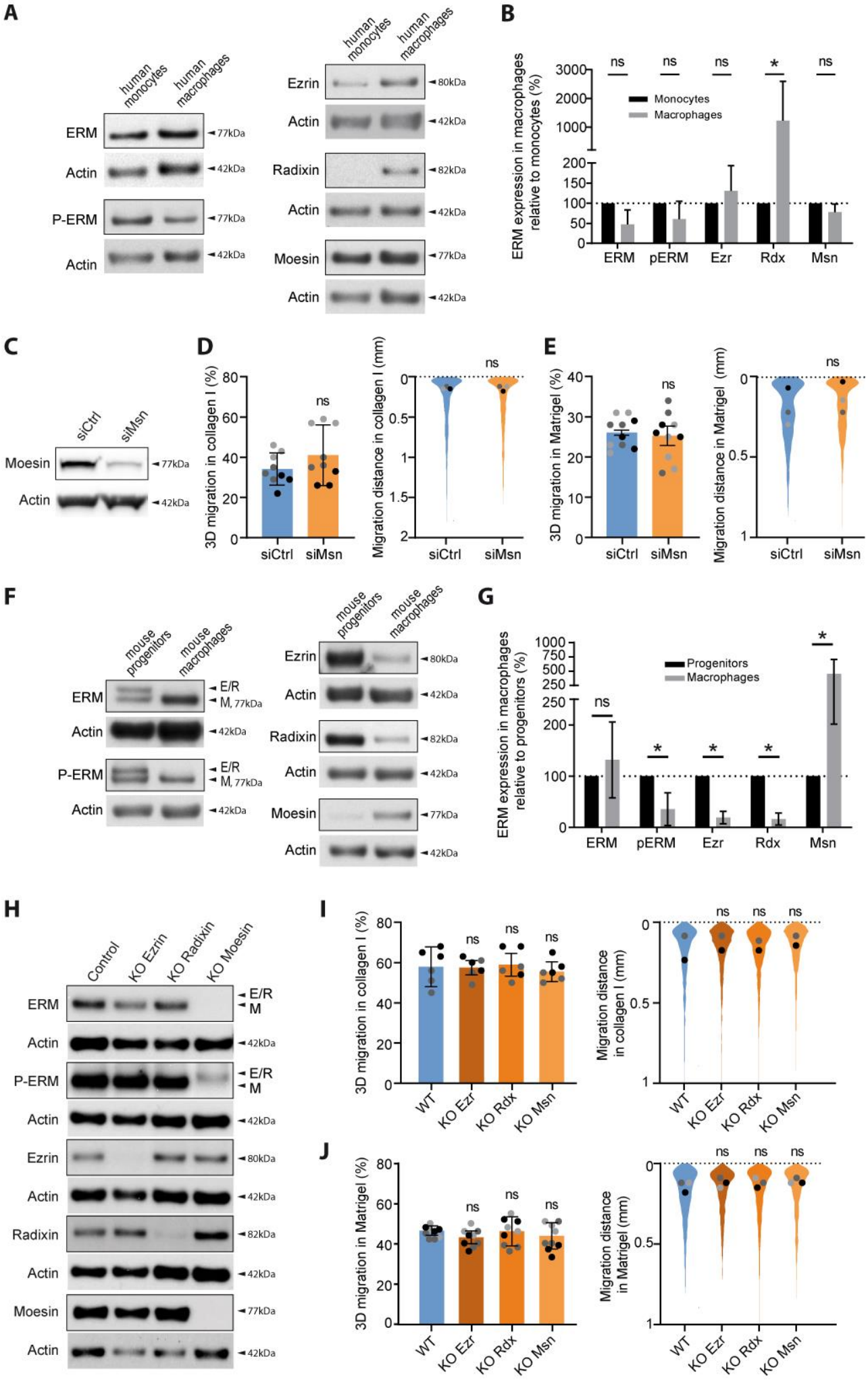

Fig. 1: Ezrin, radixin, or moesin depletion does not affect macrophage 3D migration

(A-B). Endogenous expression of ERM proteins in human myeloid cells.

A. ERM, p-ERM, ezrin, radixin and moesin expression levels of human blood-derived monocytes, and human monocyte-derived macrophages (HMDM) respectively differentiated from the same donor. Actin levels were used to normalize the immunoblots.

B. Quantification of ERM expression in macrophages relatively to monocytes was done in at least on 3 independent donors. Mean and SD are plotted. Statistics: P-values were obtained with a paired Student's t-test.

(C-E). Depletion of Moesin in human macrophages by siRNA.

C. Moesin expression level of HMDM treated with siCtrl or siMoesin (siMSN) is representative of 3 independent donors.

D-E. Percentages of migration and migration distances of siRNA-treated HMDM inside collagen I **(D)** and Matrigel **(E)** are represented as follows: the technical replicates (dot) of 3 independent experiment (highlighted by different grey colors) are represented. The mean (bar) and SD from the 3 independent experiments are shown. Statistical analysis was done on the mean per experiments using a paired two-tailed t-test. Distribution of the migration distance of each cell from 3 independent experiments is shown. Dots represent the median of each independent experiment and were used for statistical analysis using a paired two-tailed t-test.

(F-G). Endogenous expression of ERM in murine macrophages.

F. ERM, p-ERM, ezrin, radixin and moesin expression levels of murine WT hoxB8-progenitors, and WT hoxB8-macrophages.

G. Quantification of expression relatively to HoxB8-progenitors from at least 3 independent experiments. Mean and SD are plotted. Statistics: P-values were obtained with a paired Student's t-test.

H. Immunoblots showing the expression levels of ERM, p-ERM, ezrin, radixin and moesin of HoxB8-macrophages WT or respectively knockout for ezrin (KO Ezrin), radixin (KO Radixin) or moesin (KO Moesin).

(I-J). 3D migration of simple KO of ezrin-, radixin- or moesin in macrophages.

I-J. Percentages of migration and migration distances of WT, KO Ezrin, KO Radixin, or KO Moesin HoxB8-macrophages inside collagen I **(I)** and Matrigel **(J)** are plotted as follow: the technical replicates (dot) of 3 independent experiment (highlighted by different grey colors) are represented. The mean (bar) and SD from the 3 independent experiments are shown. Statistical analysis was done on the mean per experiments using a RM 1-way anova. Distribution of the migration distance of each cell from 3 independent experiments is shown. Dots represent the median of each independent experiment and were used for statistical analysis using RM 1-way anova.

Verdys et al. Figure 2

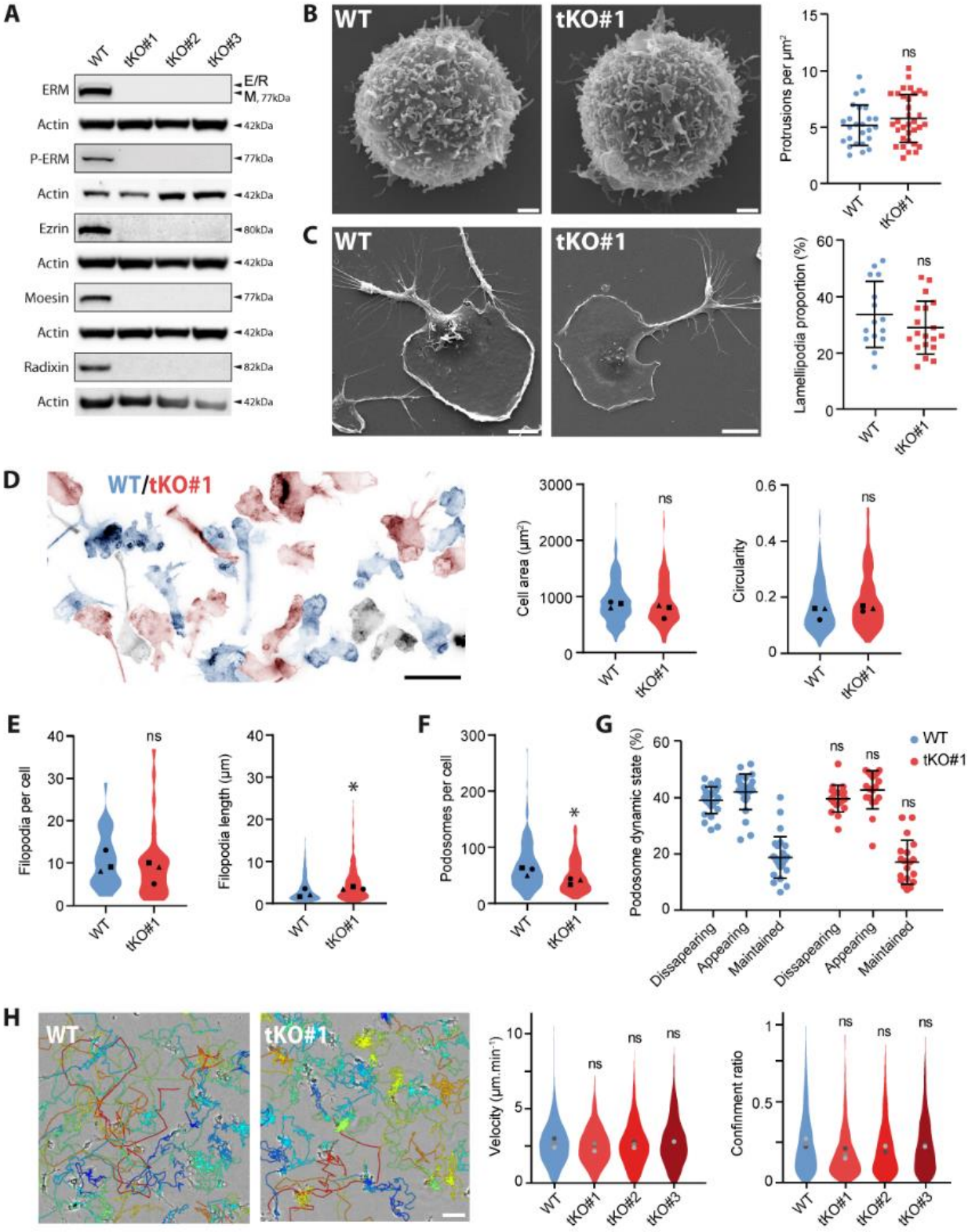

Fig. 2: ERM-tKO does not have a marked influence on the formation and dynamics of macrophage actin structures.

A. The expression levels of ezrin, radixin, moesin, ERM and p-ERM from WT Hoxb8-macrophages and three independent clones (tKO#1, tKO#2, tKO#3) triple ERM knockout (ERM-tKO) were analyzed by western blot. ERM and moesin are from the same immunoblots, that was stripped and rehybridized.

(**B-G**) Morphological analysis of ERM-tKO macrophages.

B. Morphology of WT and ERM-tKO#1 progenitors was analyzed by scanning electron microscopy (SEM) and the number of microvilli-like protrusions was quantified per μm^2 in 25 WT and 34 ERM-tKO#1 progenitors (right panel). Scale bar: 1 µm.

C. Morphology of WT and ERM-tKO#1 macrophages was analyzed by SEM and lamellipodia were evaluated as a proportion of the cell perimeter in 15 WT and 19 ERM-tKO#1 cells (right panel). Scale bar: 10 µm.

D. Actin staining of WT (blue) and ERM-tKO#1 (red) macrophages pseudo-colored according to their identification using cell trackers. Black cells, whose cell tracer staining was too weak to be identified, were removed from the analysis (left panel). Quantification of cell area (in μm^2) and circularity of 210 WT and 162 ERM-tKO#1 macrophages. The medians of 3 independent experiments are represented and used for statistical analysis (right panels). Scale bar: 20 µm.

E. Quantification of the number of filopodia per cell in 30 WT and 30 ERM-tKO#1 macrophages (left panel), and the associated filopodia length from 320 WT and 294 ERM-tKO#1 filopodia of macrophages (right panel).

F. Quantification of podosomes number of 210 WT and 162 ERM-tKO#1 hoxB8-macrophage cells.

G. Quantification of podosome stability from lifeact-GFP-expressing WT and ERM-tKO#1 macrophages plated in 2D bare glass and imaged with RIM. The dynamic states of podosomes were categorized into disappearing, appearing and maintained and expressed as percentages. See Figure S3 for detailed explanations.

H. 2D Migration of WT, ERM-tKO#1, tKO#2, and tKO#3 macrophages. Snapshot pictures showing WT and ERM-TKO#1 macrophages migrating randomly in bare glass (2D) with migratory tracks representing cell trajectories during 1h. Tracks are color coded according to their mean speed. Scale bar: 50 µm. See also movie 5. Quantification of the median velocity and the confinement ratio (0: confined movement; 1: directionally persistent movement) of each migratory track from WT, ERM-tKO#1, tKO#2, and tKO#3 HoxB8-macrophages. Violin plots represent the distribution of the analyzed parameter for all the filtered migratory tracks, and the medians of 3 independent experiments are represented and used for statistical analysis.

Verdys et al. Figure 3

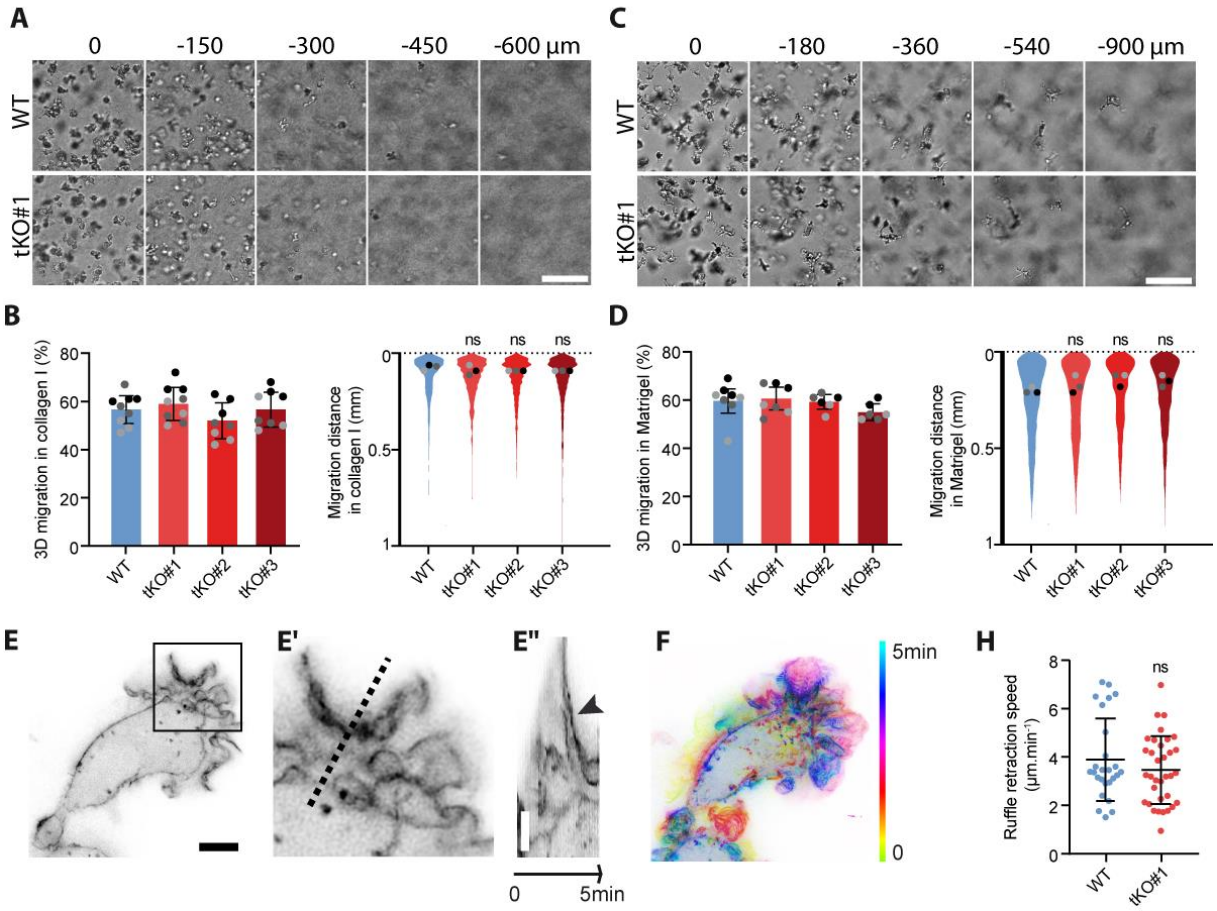

Fig. 3: ERMs are dispensable for macrophage infiltration through 3D matrices

(A, C). Morphology of WT and ERM-tKO#1 Hoxb8-macrophages inside 3D collagen I **(A)** or 3D Matrigel **(C)** is shown. Scale bars: 100 µm.

(B, D). Percentages of migration and migration distances of WT, ERM-tKO#1, tKO#2, and tKO#3 HoxB8-macrophages in collagen I **(B)** and Matrigel **(D)** are represented as follows: the technical replicates (dot) of 3 independent experiment (highlighted by different grey colors) are represented. The mean (bar) and SD from the 3 independent experiments are shown and used for statistical analysis using RM 1-way anova. Distribution of the migration distance of each cell from 3 independent experiments is shown. Dots represent the median of each independent experiment and were used for statistical analysis using RM 1-way anova.

(E-F). Acquisition of a Lifeact-GFP WT macrophage in 3D collagen I **(E)**, and timelapse color coded from 0 to 5 min for the dynamics **(F)** See also Movie 11 to compare WT and TKO cells in collagen I. Kymograph **(E'')**, following the pointed line in enlarged view **(E')**, shows the dynamics of a ruffle. Scale bars: 5 µm.

H. Quantification of ruffle retraction in the 3D collagen I matrix from 26 measures of WT and 34 of ERM-tKO#1 macrophages expressing lifeact-GFP and imaged with RIM. See also Movie 11.

Verdys et al. Figure 4

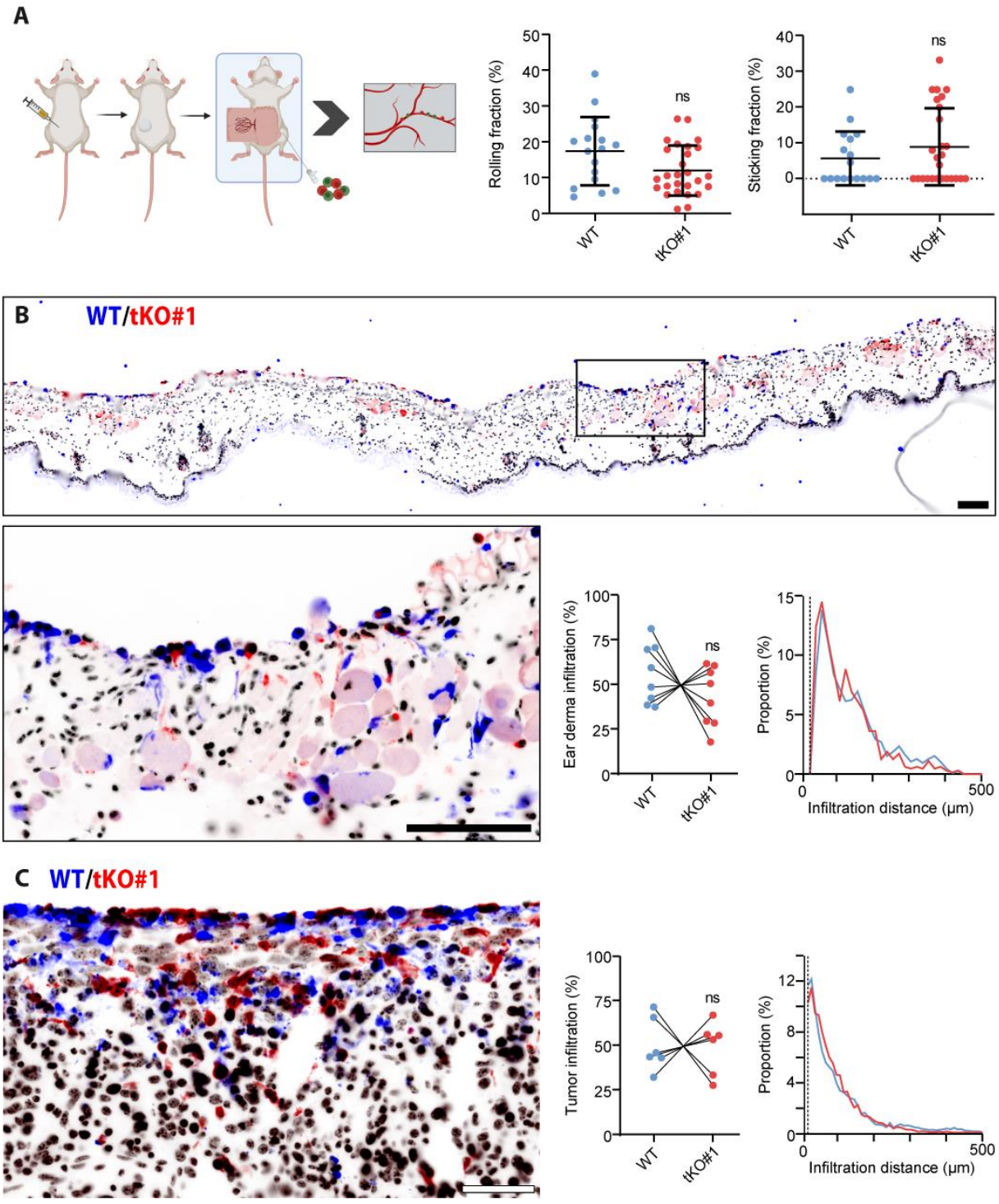

Fig. 4: ERM tKO macrophages have no defect in performing diapedesis in vivo and infiltrate tissues explants ex vivo

A. In vivo diapedesis

Fibrosarcoma cells were injected into the flank of a mice. After a week, tumor was exposed for intravital microscopy, and the femoral artery of recipient mice was catheterized for injection of exogenous cells. Differentially labeled WT and TKO-ERM HoxB8-progenitors differentiated 1 day with M-CSF were injected in the blood and the microcirculation of cells in tumor vessels was assessed by real-time imaging. Rolling fractions were quantified as the percentage of rolling cells in the total flux of cells in each blood vessel, and sticking fractions were quantified as the percentage of rolling cells that firmly adhered for a minimum of 30 seconds.

B. *Ex vivo* infiltration of ear derma

Differentially labeled WT and tKO#1 macrophages were seeded on top of a murine ear derma tissue over 3 days. Slices were then fixed and serial sectioning was performed along the z-axis. Immuno-histofluorescence of an ear section showing WT (blue) and tKO#1 (red) macrophage infiltration and dapi staining of all nuclei (black). Quantifications of the percentage and the distance of ear derma infiltration of WT or tKO#1 macrophage is represented as the mean of the respective infiltration percentage per ear halve section. Analysis was performed on 7 independent ear halve explants from 4 mice. Scale bars: 50 µm.

C. *Ex vivo* infiltration of tumor explants

Differentially labeled WT and tKO#1 HoxB8-macrophage cells were seeded on top of sliced fibrosarcoma explants over 3 days. Slices were then fixed and serial sectioning was performed along the z-axis. Immuno-histofluorescence of a tumor section showing WT (blue) and tKO#1 (red) macrophage infiltration and dapi staining of all nuclei (black). Quantifications of the percentage and the distance of tumor infiltration of WT or tKO#1 macrophages are represented. Means of 6 *ex vivo* independent tumor explants from 3 tumors are shown. Representative pictures are shown. Scale bars: 50 µm.

Of note, cell trackers used to stain the cells were switched between all experiments to verify the absence of effects due to staining.

Verdys et al. Figure 5

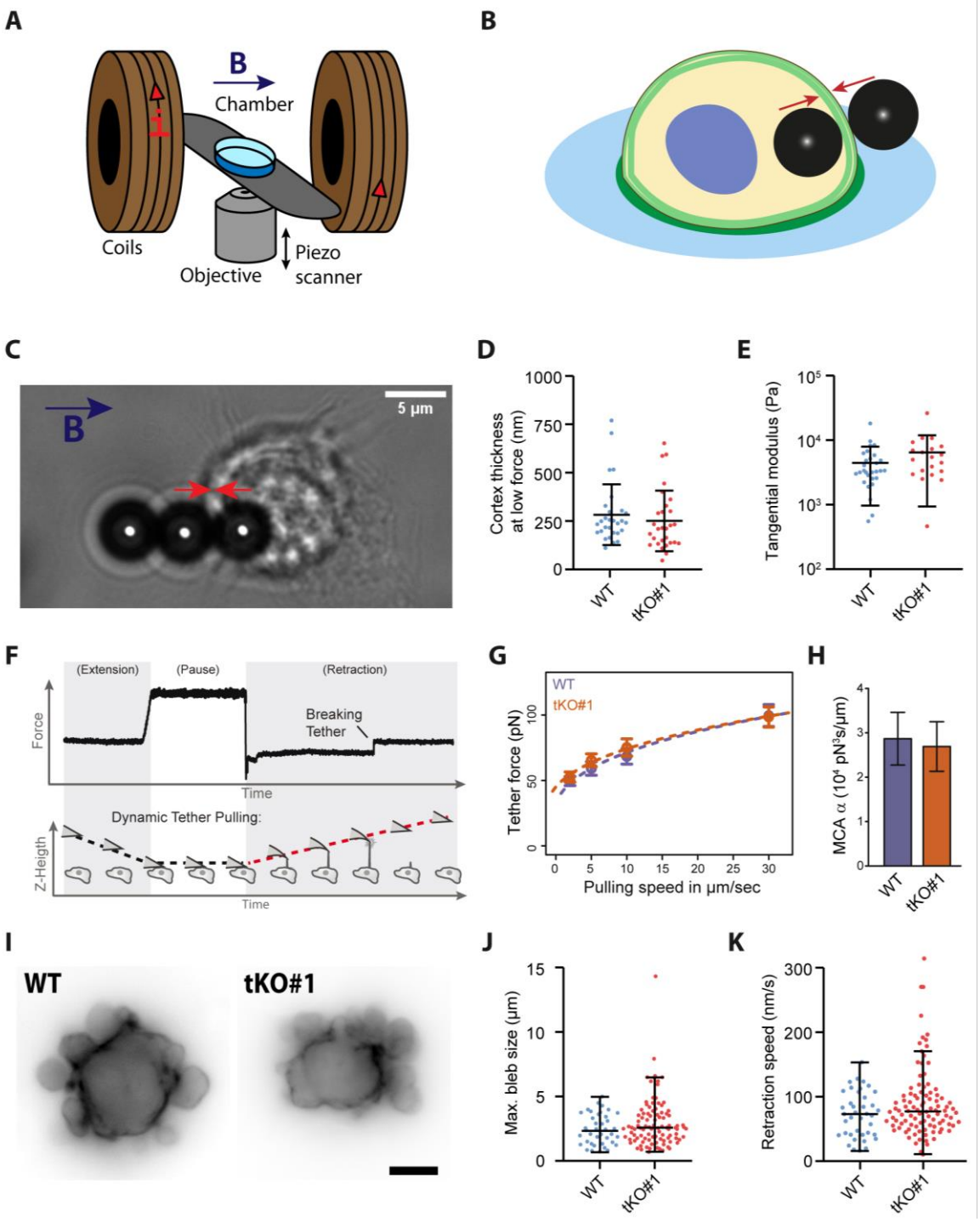

Fig. 5: ERM depletion does not affect macrophage cortex thickness and stiffness.

(A-B). Scheme of the magnetic setup for the cortex pinching experiment: an inverted microscope is associated with two coaxial coils to generate a quasi-homogeneous magnetic field, B, in the sample region **(A)**. Through the application of a magnetic field, beads align, and the cortex is pinched between a bead inside the cell and a bead outside the cell **(B)**.

C. Bright-field image of a WT HoxB8 macrophage, with one internalized and two external magnetic beads aligned by a magnetic field. Scale bar: 5 µm.

D. Median of the cortical thickness of WT and ERM-tKO#1 macrophages were measured by applying a low force (5 mT) between two magnetic beads.

E. Cortical stiffness response are represented by the tangential elastic modulus at low stress between 150 and 350 Pa.

F. Exemplary force curve from atomic force spectroscopy operated in dynamic tether pulling mode. Tethers break while the cantilever is retracted at a defined velocity with the Z-height increasing constantly.

G. Force-velocity curve from dynamic tether pulling on CTL and ERM-TKO HoxB8 macrophages. Data points are mean tether force f±SEM at 2, 5, 10 and 30 µm/sec pulling velocity. At least 16 cells per condition were analyzed in 4 independent experiments.

H. Mean and standard deviation of the MCA parameter Alpha obtained from fitting the Brochard-Wyart model (see Methods for details). No statistical difference was observed (p-Value (Z-test): 0.83).

I. Blebbing of Lifeact-mCherry WT and Lifeact-GFP ERM-tKO progenitor cells after incubation with 10% distilled H_20 to induce hypo-osmotic stress.

J. Quantification of the maximum bleb size per blebbing WT and ERM-tKO progenitors extracted from short-time widefield movies.

K. Quantification of the retraction speed of blebs from short-time widefield movies.

Verdys et al. Suppl. Fig. S1

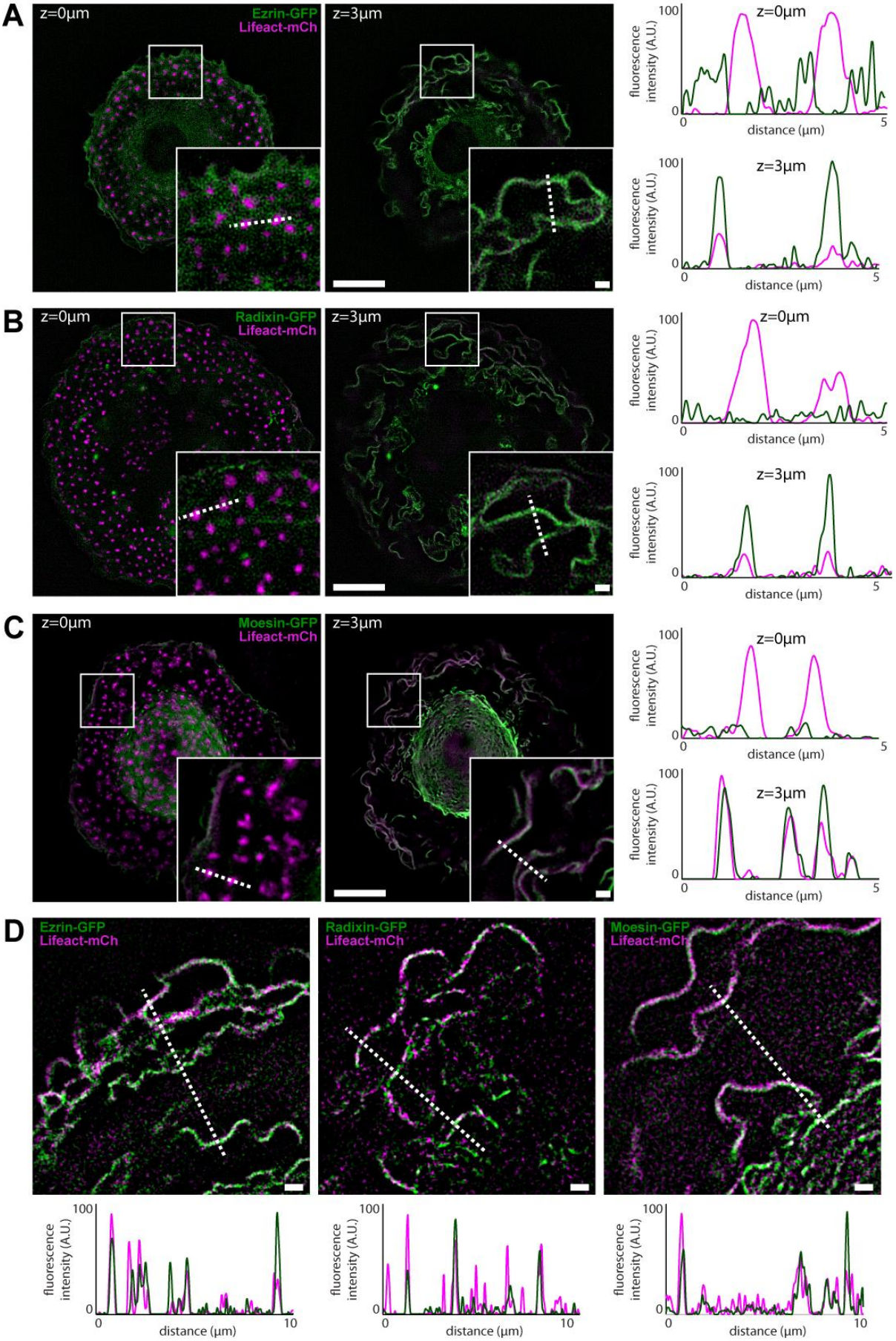

Fig. S1: Localization of Ezrin, Radixin and Moesin proteins in human macrophages

A-C. Representative SIM images of HMDM co-transfected with ezrin-GFP (green) **(A),** radixin-GFP (green) **(B)** or moesin-GFP (green) **(C)** and Lifeact-mCherry (magenta) at the basal membrane, showing podosomes (z=0 µm) and at 3 µm above the basal membrane, showing membrane ruffles (left panels). Scale bars: 10 µm, enlarged view: 1 µm. Intensity profiles along the dotted line from both enlarged view of left panels, crossing podosomes (z=0 µm) and membrane ruffles (z=3 µm) (right panels). Also see z-stack movies 1, 2 and 3. The fluorescence levels were adjusted in the same way in order to compare the intensity at the base of the cells to the upper planes. Note that ERM are mainly accumulated in the upper ruffles, compared to the basal plasma membrane and that only Ezrin slightly accumulate around podosome cores.

D. Enlarged view of ruffle dynamics from SIM images of HMDM co-transfected with ezrin-GFP (left panel), radixin-GFP (middle panel) or moesin-GFP (right panel) (green) and Lifeact-mCherry (magenta). Scale bars: 1 µm. ERM-GFP (green) or actin (magenta) intensity profiles along the dotted line are plotted below. Note that peripheral ruffles are enriched in F-actin, whereas ERM are present in both peripheral and central ruffles. Also see time-lapse movies 1, 2 and 3.

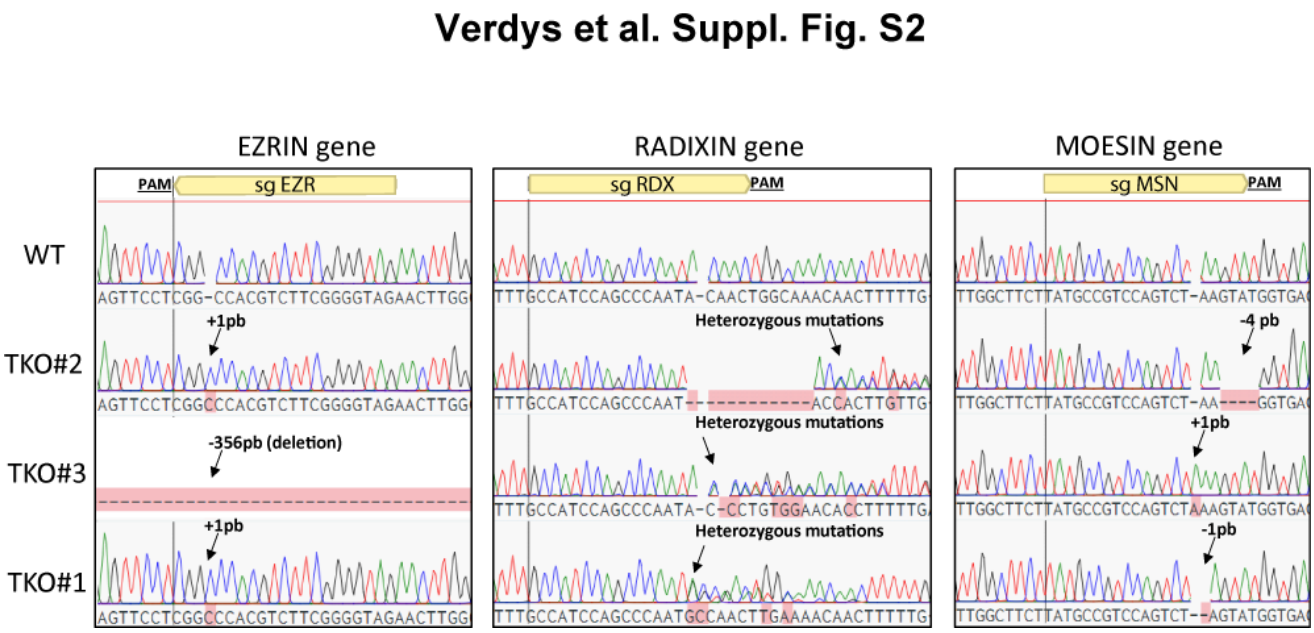

Fig. S2: ERM-tKO clones have genomic mutations on each 3 ERM genes

Sequence analysis of genomic DNA mutations of the three ERM-tKO clones (tKO#1, tKO#2, and tKO#3) in ezrin, radixin and moesin genes. Targeted sgRNAs and PAM are depicted.

Verdys et al. Suppl. Fig. S3

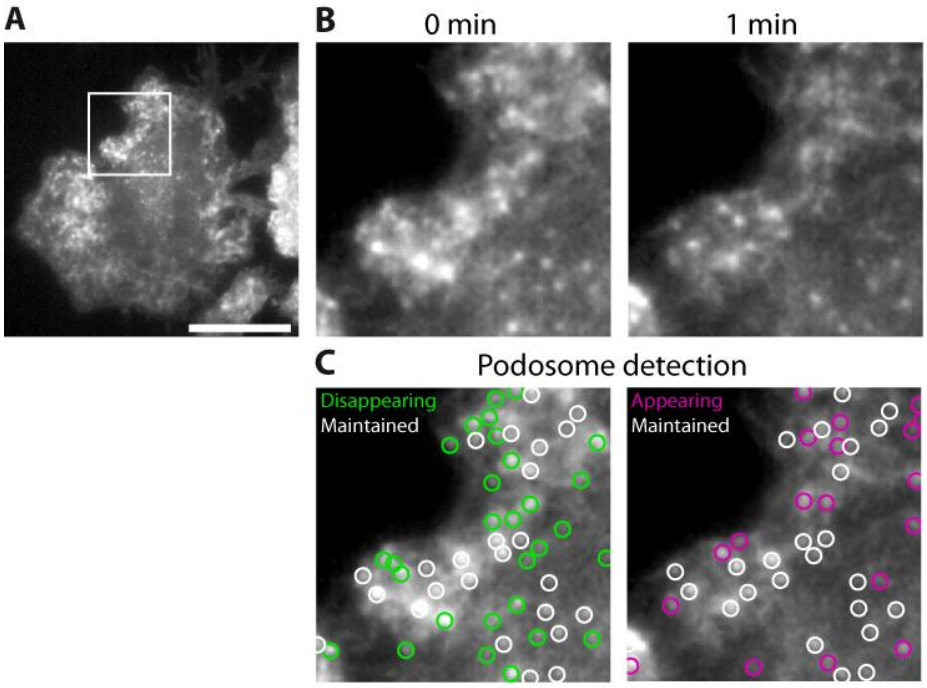

Fig. S3: Quantification of podosome stability on RIM videos.

We designed an in-house imageJ macro to extract podosome stability from RIM videos of WT and ERM-tKO macrophages expressing lifeact-GFP **(A)**. Briefly, one image per minute was selected for the first 3 minutes of the video (B), then podosome location and shape was extracted and a “Maxima Within Tolerance” mask was generated. The comparison between consecutive masks allowed podosome classification into three categories (Appearing, disappearing and maintained) depending in their presence at first, second or both images (C).

Verdys et al. Suppl. Fig. S4

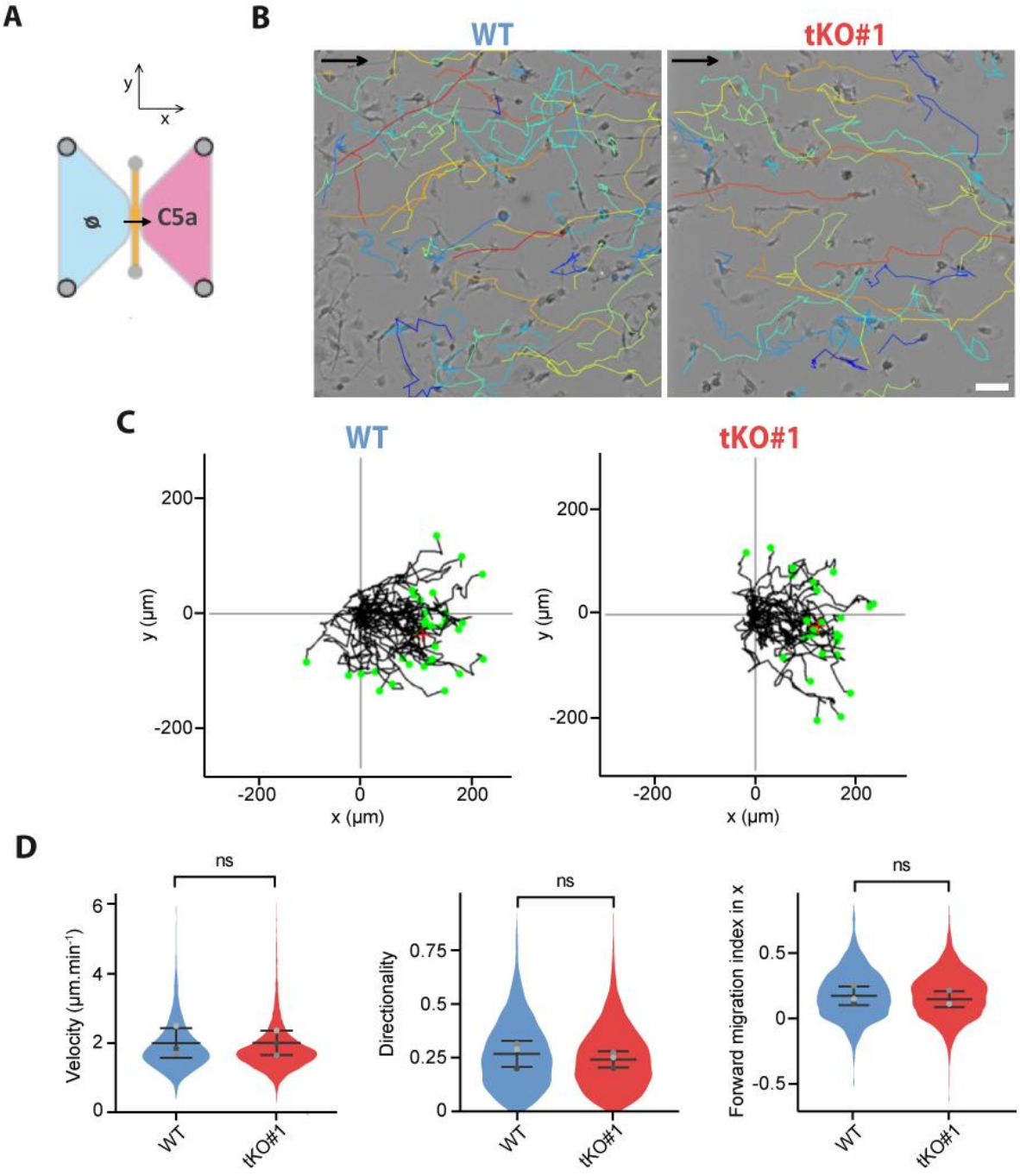

Fig. S4: 2D chemotaxis of WT and ERM-tKO#1 macrophages toward a C5a gradient

A. Schematic representation of 2D chemotaxis assay toward C5a. WT and ERM-tKO#1 cells migrating along a C5a gradient in the x axis. See also movie 6.

B. Snapshot of WT and ERM-tKO#1 macrophages migrating toward C5a gradient (on the right) with migratory tracks representing cell trajectories during 90min. Tracks are color coded according to their directionality. Scale bar: 50µm.

C. Migratory tracks of WT and ERM-tKO#1 macrophages with origins set at (0,0).

D. Quantification of the median velocity, the directionality, and the forward migration index in the x axis (FMIx, used as a chemotaxis indicator) of each migratory track. The medians of 3 independent experiments are represented and used for statistical analysis.

Legends of the movies

Movie 1: SIM Z-stack images of Ezrin-GFP (green) and Lifeact mCherry (magenta) co-transfected in HMDM.

Movie 2: SIM Z-stack images of Radixin-GFP (green) and Lifeact mCherry (magenta) co-transfected in HMDM.

Movie 3: SIM Z-stack images of Moesin-GFP (green) and Lifeact mCherry (magenta) co-transfected in HMDM.

Movie 4: SIM timelapse movies showing podosomes structures at the basal membrane (left), and membrane ruffles (right) of Ezrin-GFP (green) and Lifeact mCherry (magenta) co-transfected in HMDM.

Movie 5: SIM timelapse movies showing podosomes structures at the basal membrane (left), and membrane ruffles (right) of Radixin-GFP (green) and Lifeact mCherry (magenta) co-transfected in HMDM.

Movie 6: SIM timelapse movies showing podosomes structures at the basal membrane (left), and membrane ruffles (right) of Moesin-GFP (green) and Lifeact mCherry (magenta) co-transfected in HMDM.

Movie 7: Podosomes dynamics through acquisitions by RIM of WT (top) and ERM-tKO (bottom) lifeact-GFP macrophages plated on 2D glass. Time format in min:sec.

Movie 8: 2D random migration of WT and ERM-tKO macrophages with migratory tracks representing cell trajectories. Tracks are color coded according to their mean speed. Time format in h:min.

Movie 9: 2D chemotaxis of WT and ERM-tKO macrophages toward a C5a gradient with migratory tracks representing cell trajectories. Tracks are color coded according to their directionality. Time format in h:min.

Movie 10: Top-to-bottom Z-stack of WT and ERM-tKO macrophages infiltrating a 3D collagen I matrix.

Movie 11: Top-to-bottom Z-stack of WT and ERM-tKO macrophages infiltrating a 3D Matrigel matrix.

Movie 12: Movie of WT and ERM-tKO macrophages migrating in Collagen I. Scale bar: 50µm. Time format in h:min.

Movie 13: Movie of WT and ERM-tKO macrophages migrating in 3D Matrigel. Time format in h:min.

Movie 14: Acquisition of lifeact-GFP WT macrophages (top), and ERM-tKO#1 macrophages (bottom) in 3D collagen I. Time format in min:sec.

Movie 15: Acquisition of lifeact-GFP WT macrophages (top), and ERM-tKO#1 macrophages (bottom) in 3D Matrigel. Time format in min:sec.

Movie 16: Movie of WT and ERM-tKO progenitor cells blebbing after incubation with 10% H_20.